Università degli Studi di Messina

Dipartimento di Scienze Matematiche e Informatiche,
Scienze Fisiche e Scienze della Terra

Doctoral Programme in "Physics" XXXV Cycle

Analytical and Numerical Approaches for Light Scattering by Nanostructured Materials

Doctoral Thesis of:

Abir SAIDI

Supervisor:

Prof. Rosalba SAIJA

Co-Supervisor:

Dr. Maria Antonia IATÌ

Ph. D. Course Coordinator:

Prof. Vincenza CRUPI

Academic Year 2021 - 2022

Contents

Chapters

Introduction

Light scattering and absorption are ubiquitous phenomena with a strong impact on our everyday life. Light scattering includes a whole class of light-matter interaction processes during which light is deflected due to the interaction with an obstacle. Most of our visual perceptions result from the scattering and absorption of light by the objects around us. Colors, brightness, and glossiness are a consequence of different scattering and absorption properties.

Due to its strong impact, light scattering has been and still is an important research field in physics. The Maxwell equations describing the nature of electromagnetic waves, dated back to the 1860's, are the basis of the electromagnetic theory and the fundamental tool for the understanding of light scattering and absorption processes.

We can distinguish between elastic scattering when no energy transfers are involved in the process and inelastic otherwise. Rayleigh scattering and Mie scattering belong to the first category, while a typical example of inelastic scattering is Raman scattering. In this thesis, only the case of elastic scattering will be considered because, in the matter-radiation interactions under study, the energy is conserved. A complete study of the problem can be done using Quantum Electrodynamics. However, in the cases of our interest, we can neglect quantum contributions and use a fully classical description.

Historically, light scattering in the classical theoretical understanding has been investigated through suitable approximations that depend on the particle size [1]. For homogeneous spherical particles, an accurate evaluation of the radiation fields can be obtained by Mie theory [2] [3]. When we consider scattering processes involving non-spherical or non-homogeneous particles, we need to use more sophisticated approaches. The Transition matrix (T-matrix) has proven to be one of the most powerful methods to solve the light scattering problem by cluster or aggregates of spherical monomers, by spheres with spherical, possibly eccentric, inclusions, and nano-shell particles [4]. The T-matrix formalism, first derived by Waterman [5], is based on the multipole expansions of the electromagnetic fields and on the calculation of the linear Transition operator that, acting on the multipole amplitudes of the incident field, gives as a result the multipole amplitudes of the scattered field. It can be regarded as a generalization of Mie theory, to which it reduces for a single homogeneous spherical particle. Although the analytical approach of the multipole expansion is relatively simple and general, the computational methods needed to calculate the expansion coefficients from the imposition of the boundary conditions on the surface of the scatterer can be quite complex [4].

The T-matrix gives the opportunity to explore several systems and configurations in a broad range of fields of applications, such as interstellar dust modelling [6], light trapping in complex fractal structures [7], plasmonics, and optical trapping [8] see figure 1. We will describe this method in detail and also compare it with alternative approximated approaches that, only in specific regimes, can grant a fast and simple way to obtain reasonable results.

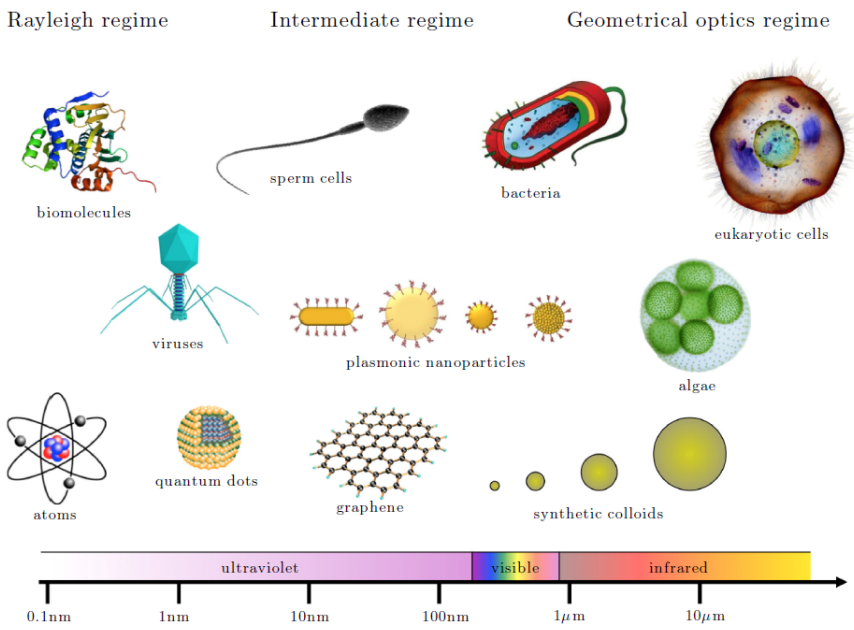

Figure 1: Trapping regimes and typical objects that are trapped in optical manipulation experiments. In defining the regimes of optical trapping, we have assumed trapping wavelengths that fall in the visible or near-infrared spectral region [1].

In recent years the T-matrix method has been successfully applied to the study of the mechanical effects of light, proving to be a very efficient tool to calculate optical forces, especially in the case of non-spherical particles or at intermediate size scale, where approximate descriptions are bound to fail. Optical forces emerge from momentum exchange between light and matter and play a key role in optical trapping and manipulation (optical tweezers). This is an ever growing research field with relevant applications in biology, medicine, nanofluidics, soft matter, atomic physics, and photonics, just to mention a few [9].

Despite the relevant advances in optical trapping techniques and the key role

played by radiation pressure in many cosmic processes, the application of optical tweezers to space exploration and cosmic dust characterization (space tweezers) has yet to be developed. The application of optical trapping to space materials is challenging and paves the way for a new research field. In space missions, several techniques have been developed to collect and characterize extra-terrestrial samples, but with the drawback of unavoidable sample contamination. Optical trapping systems mounted on stratospheric instruments, onboard cometary probes, or on rovers to Mars or to the Moon would mean the opportunity for *in situ* characterization of extraterrestrial material without any contamination.

This thesis is organized as follows. In the first chapter, we introduce the light scattering theory. After a preliminary discussion on the different scattering regimes meant to motivate the use of approximated approaches under certain conditions, we illustrate some methods to solve the light scattering problem. First, we introduce the T-matrix technique, a rigorous analytical method based on a complete electromagnetic theory. Then, the dipole approximation with its limits of applications and, finally, the numerical approaches, specifically the Finite Difference Time Domain method (FDTD).

In the second chapter, we present the theory of optical forces and optical tweezers. After introducing the Maxwell stress tensor and the general equations from which optical forces and torques can be calculated [10], we describe how the T-matrix approach can be used to calculate optical forces efficiently. Then, we compare this description with those obtained using the dipole approximation and the FDTD,

showing the implementation of computing codes with the three different approaches.

The third chapter presents and discusses a comparison between analytical and numerical approaches to calculate the optical forces for some representative case studies, specifically single spherical particles and dimers. Results obtained through the T-matrix, the FDTD approach, as implemented in Lumerical, and the Dipole approximation will be shown in order to compare the strengths and weaknesses of the various computational approaches.

In the fourth chapter, we discuss the application of optical tweezers to space exploration and cosmic dust characterization. We present the results obtained for the optical forces acting on cosmic dust analogs using the T-matrix method, highlighting the key role played by dust composition and morphology for optical trapping. Finally, the perspectives for future and challenging applications of optical tweezers in curation facilities for sample return missions or in extraterrestrial environments will be discussed [11, 6].

In the last chapter, we present an application of the T-matrix method in plasmonics to study the optical properties of Ag-Au colloidal alloys produced by pulsed laser ablation in liquid [12].

Chapter 1

The Scattering Problem: analytical and numerical approaches

The scattering problem aims at describing the electromagnetic fields scattered by a particle when it is illuminated by an incoming electromagnetic wave.

1.1 Scattering Regimes

Approximated solutions to the scattering problem can prove very valuable in specific situations when the particle size is very small or very large compared to the wavelength of the light. A striking example is given by optical trapping calculations that are often applied to dielectric nanoparticles or to particles of tens of microns, much smaller or much larger than the visible wavelength used to trap them, respectively [1]. Approximations are often much easier to handle with respect to full electromagnetic calculations. However, they are inapplicable when dealing with systems with a size comparable to the light wavelength or with a highly non-spherical shape.

When limiting to spherical particles, we can identify regimes that depend on the particle radius. For each regime, simplifications and approximations are made for a fast but often qualitative understanding and calculation of the light scattering

properties. The *size parameter* x is crucially used to determine the range of validity of these approximations:

$$x = k_m a = \frac{2\pi n_m}{\lambda_0} a$$

Where k_m is the light wavenumber in the medium surrounding the particle, λ_0 is the incoming monochromatic wavelength in vacuum, a is the particle radius, and n_m is the refractive index of the surrounding non-magnetic medium.

When the particle radius is much larger than the incident wavelength ($k_m a >> 1$), we can safely use a theoretical approach based on the ray optics regime. In the opposite case, if the radius of the particle is much smaller than $k_m a$, we can use the Rayleigh approximation and consider the particle as a dipole or a suitable collection of dipoles [1]. This means that we consider the electromagnetic field homogeneous inside the particle under the condition $|n_p/n_m| k_m a << 1$ where n_p is the refractive index of the particle.

In case $k_m a \approx 1$, we need to use complete wave-optical modelling of the particle-light interaction to calculate the cross sections and the mechanical effects of light. In such a case, the T-matrix approach proves to be a very convenient choice, as far as it is possible to take advantage of the symmetry of the particle responsible for light scattering. Several techniques, mostly numerical, are based on a rigorous electromagnetic theory and, in some cases, can take into account the precise shape of the particle. In this respect, we first remember the extended boundary conditions methods, mainly based on the pioneering paper of Waterman [5], that rely on integrals over the volume or over the surface of the particle. If these integrals can

be calculated, at least numerically, with sufficient accuracy, these methods account very well for the actual shape of the particle. Secondly, we recall the so-called finite elements methods, which have in common the spatial or temporal discretization of the scattering problem, leading to the replacement of spatial and temporal derivatives in Maxwell's curl equations by finite difference quotients.

In the following sections, we introduce the mathematical formalism of the multipole fields for the description of electromagnetic fields, which leads to the analytic definition of the *Transition matrix*. We show how powerful this method is for describing scattering by non-spherical particles, modelled as cluster of spheres. Then, we present one of the most common finite methods in the time domain, the Finite Difference Time Domain method (FTDT), as implemented by Lumerical, and, finally, we discuss the range of application of the dipole approximation to be able to compare the potential and limitations of the three different approaches.

1.2 Analytical and numerical approaches

Although eminent scientists had already dealt with the problem (Debye, Lorenz, Clebsch,...), the first fundamental work on light scattering by spherical particles was written by Gustav Mie and published in 1908. Mie solved the problem by giving a rigorous analytical solution by studying the scattered light in a colloidal solution made of spherical golden particles [2].

The geometry of the problem is illustrated in figure 2. Here, we consider a homogeneous particle of refractive index n_p in a medium of refractive index n_m. If the incident electric field is $\vec{E}_i(\vec{r})$ and we denote the scattered electric field as $\vec{E}_s(\vec{r})$, the total electric field outside the particle is $\vec{E}_t(\vec{r})$=$\vec{E}_i(\vec{r})$+$\vec{E}_s(\vec{r})$. We will indicate the total electric field inside the particle $\vec{E}_p(\vec{r})$.

The starting point is the solution of Maxwell's equations:

$$\nabla \cdot \vec{D} = \rho$$

$$\nabla \cdot \vec{B} = 0$$

$$\nabla \times \vec{H} - \frac{\partial \vec{D}}{\partial t} = \vec{J}$$

$$\nabla \times \vec{E} + \frac{\partial \vec{B}}{\partial t} = 0$$

Supplemented by the constitutive equations that relate the field vectors to each other within a given medium. As far as we dealt with linear media, the constitutive

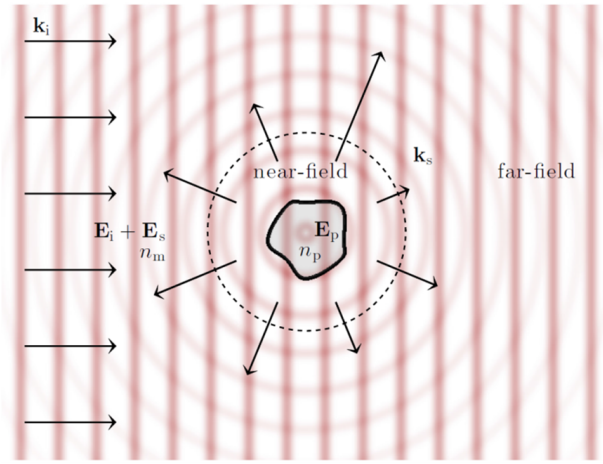

Figure 2: Pictorial view of the scattering process. Scattering theory studies how an incoming electromagnetic wave is scattered by a particle. In general, when light impinges on an object, the object emits a scattered electromagnetic field, which in the far field is a spherical wave. In particular, given an incoming linearly polarised plane electromagnetic wave ($\vec{E}_i(\vec{r})$) in a medium of refractive index n_m impinging on a particle of homogeneous refractive index n_p, one wants to determine the electromagnetic field inside the particle($\vec{E}_p(\vec{r})$) and the scattered electromagnetic field ($\vec{E}_s(\vec{r})$), both in the near field and in the far field [1].

equations are:

$$\vec{D} = \epsilon\vec{E}, \vec{B} = \mu\vec{H}, \vec{J} = \sigma\vec{E}$$

where ϵ, σ, and μ, thanks to the assumed linearity of the media, are tensors whose components are independent of the field strength. Moreover, as the media we are considering are non-magnetic and isotropic, $\mu = 1$ and ϵ and σ reduce to scalars that, in the case of non-homogeneous media, are space-dependent.

The linearity of the field equations and of the constitutive relations allows us to apply them to each of the monochromatic components obtained through a time

Fourier transform of the fields. Through a straightforward analytic procedure, it is possible to transform the system consisting of the four Maxwell differential equations into the pair of decoupled vector Helmholtz equations:

$$(\nabla^2 + n^2 k_0^2)\vec{E} = 0$$

$$(\nabla^2 + n^2 k_0^2)\vec{B} = 0$$

where:

$$n_m^2 = \mu\left(\epsilon + \frac{4\pi i\sigma}{ck_0}\right)$$

is the complex refractive index of the medium in which the field propagates, where the positive sign in front of the imaginary part of n^2 is due to the choice of the time dependence as exp(-iwt), with $w = ck_0$

The solution of these vector differential equations would certainly be easier if rectangular coordinates were used, but this choice appears advantageous only when the separation surfaces between the media through which the field propagates are plane. In this case, each of the vector Helmholtz equations separates into a set of scalar ones that acts on the single component of the electric and/or magnetic field.

In any other case, to achieve this advantageous decoupling, it is necessary to find another coordinate system that respects the symmetry of the system.

Regardless of the geometry of the system, the physically significant solutions of the Helmholtz equations must still meet the boundary conditions applied to the

separation surface between the outer medium and the scatterer:

$$\vec{n} \times (\vec{E_1} - \vec{E_2}) = 0$$

$$\vec{n} \times (\vec{B_1} - \vec{B_2}) = 0$$

where $\vec{n}$ is the versor normal to the separation surface. The analytical formulation of the boundary conditions will also benefit from the choice of an appropriate coordinate system according to the symmetry of the scatterer.

1.3 Multipole Fields and Transition Matrix Formalism

1.3.1 General Solutions of Helmholtz equation

Let us consider the Helmholtz equation in its scalar form:

$$(\nabla^2 + k_v^2)F(\vec{r}) = 0$$

where $F(\vec{r}) = F(r, \theta, \phi)$ represents a component of the electromagnetic field. Assuming that the symmetry of the problem is spherical, this differential equation can be easily solved by writing it in spherical coordinates and taking into account that the scalar function $F(\vec{r})$ can be factored as $F(\vec{r}) = F(r)\Phi(\psi)\Theta(\theta)$. The angular solution of the

scalar Helmholtz equation is given in terms of spherical harmonics Y_{lm} [10, 13]:

$$Y_{lm}(\hat{r}) = Y_{lm}(\theta, \phi) = \Theta(\theta)\Phi(\psi) = \sqrt{\frac{2l+1}{4\pi}\frac{(l-m)!}{(l+m)!}}P_{lm}(\cos\theta)e^{im\psi}$$

which on a unitary sphere form an orthonormal basis of scalar functions. As for the radial part of the $F(r)$, it can be shown that there are two linearly independent solutions that satisfy the equation, the Bessel spherical functions[10, 13] which have the property of being regular at the origin:

$$j_l(z) = (-z)^l \left(\frac{1}{z}\frac{d}{dz}\right)^l \frac{\sin z}{z}$$

and the Hankel spherical functions [10, 13] of the first kind that satisfy the radiation condition at infinity,

$$h_l(z) = h_l^{(1)}(z) = j_l(z) + y_l(z)$$

The solution of the scalar equation discussed above is of fundamental importance since all the vector fields involved in a scattering process satisfy the Helmholtz equation and, if the symmetry of the system allows it, can be resolved analytically for each of their scalar components. However, the EM field is a vector field, and this quality must also be maintained in the solutions of the equations to correctly describe all phenomena related to polarization, a crucial physical characteristic in the correct description of the field. For this reason, it is necessary to use the vector

spherical harmonics [10, 13] as follows:

$$\vec{X}_{lm} = \frac{1}{\sqrt{l(l+1)}}(-i\vec{r} \times \nabla)Y_{lm} = \frac{1}{\sqrt{l(l+1)}}\vec{L}Y_{lm}$$

These vectors form an orthonormal basis on which we can represent the electromagnetic field that propagates in a homogeneous media and constitute the spherical multipole fields on the basis of which we decide to develop all the fields involved in the scattering process.

In particular, we define J-multipoles, the vectors used for the construction of the regular fields at the origin:

$$\vec{J}^{(1)}_{lm} = j_l(kr)\vec{X}_{lm}(\hat{r}), \vec{J}^{(2)}_{lm} = \frac{1}{k}\nabla \times \vec{J}^{(1)}_{lm} \tag{1}$$

and H-multipoles that go to zero when r tends to $infinity$:

$$\vec{H}^{(1)}_{lm} = h_l(kr)\vec{X}_{lm}(\hat{r}), \vec{H}^{(2)}_{lm} = \frac{1}{k}\nabla \times \vec{H}^{(1)}_{lm} \tag{2}$$

The superscript $p = 1, 2$ is a parity index that distinguishes the magnetic multipole fields($p = 1$) from electric ones ($p = 2$). Note that the multipole fields are the solution to the Maxwell equations and eigenvectors of L^2 and L_z as well as of the parity.

1.3.2 Multipole expansions of Electromagnetic Fields

In this section, we deal with the expansion of the electromagnetic incident and scattered fields in terms of multipole fields. Without loss of generality, we can consider that the incident field is constituted by a plane wave propagating in an *homogenous* media, with refractive index n_m and propagation vector $\vec{k}$; in this case, one of the monochromatic components of the time Fourier transform of the field EM fields is represented by the following equations:

$$\vec{E} = E_{0\eta}\hat{e_\eta} exp(i\vec{k_m} \cdot \vec{r}) \tag{3}$$

$$i\vec{B} = in_m E_{0\eta}(\hat{k_m} \times \hat{e_\eta}) exp(i\vec{k_m} \cdot \vec{r}) \tag{4}$$

where $|k_m| = n_m|k_0|$ and $\hat{e}_\eta$ represents one of the two possible states of field polarization. As stated in the preceding section, the multipole field 1-2, solution of Helmholtz equation in free space, are written in terms of vector spherical harmonics $\vec{X}_{lm}$ that constitute an orthonormal basis on which the EM field can be expanded, for this reason, we get the following:

$$\vec{E_i} = \sum_{\eta=1}^{2} E_{0\eta} \sum_{l=0}^{+\infty} \sum_{m=-l}^{+l} W_{lm}^{(1)}(\hat{e}_\eta; \hat{k}) \vec{J}_{lm}^{(1)}(k_m, \vec{r}) + W_{lm}^{(2)}(\hat{e}_\eta; \hat{k}) \vec{J}_{lm}^{(2)}(k_m, \vec{r}) \tag{5}$$

$$i\vec{B_i} = n_m \sum_{\eta=1}^{2} E_{0\eta} \sum_{l=0}^{+\infty} \sum_{m=-l}^{+l} W_{lm}^{(2)} \vec{J}_{lm}^{(1)}(k_m, \hat{r}) + W_{lm}^{(1)} \vec{J}_{lm}^{(2)}(k_m, \hat{r}) \tag{6}$$

where we have used J-multipole fields that are regular at the origin. The coefficients of the incident fields are known and can be analytically determined by applying the orthogonality relations of the vector spherical harmonics:

$$E_{0\eta} W_{lm}^{(1)} j_l(kr) = \int \vec{E} \cdot \vec{X}_{lm}^{*} d\Omega = 4\pi i^l E_{0\eta} \hat{e_\eta} \cdot \vec{X}_{lm}^{*}(\hat{k})$$

$$n_m E_{0\eta} W_{lm}^{(2)} j_l(kr) = i \int \vec{B} \cdot \vec{X}_{lm}^{*} d\Omega = 4\pi i^{l+1} E_{0\eta} (\hat{k} \times e_{\{}\hat{e}ta) \cdot \vec{X}_{lm}^{*}(\hat{k})$$

In close analogy with the incident field, the scattered field has a similar form but for the multipole fields type; in fact, we have to use H-multipole, equation 2, that have the suitable properties at ∞:

$$\vec{E_s} = \sum_{l=0}^{+\infty} \sum_{m=-l}^{+l} A_{lm}^{(1)} \vec{H}_{lm}^{(1)}(k_m, \hat{r}) + A_{lm}^{(2)} \vec{H}_{lm}^{(2)}(k_m, \hat{r}) \tag{7}$$

Series like those in the equations 5-7 have infinite terms, but there is an optimal value of l, say L, to which you can truncate the series and be sure that it converges. This criterion meets a more precise empirical formula found by Wiscombe (1979) [14], that however is not suitable for metal nanoparticles. In this case, we choose to truncate the multipolar expansion requiring that the values of scattering, absorption , and extinction cross-section have an accuracy of one part in a million evaluated between two jobs running with different L values. It has been shown that, for a system with a size parameter x and a refractive index typical of a dielectric material, it is sufficient to include in the series terms with l of just over the integer part of x

[13].

1.3.3 Transition matrix

As stated above, the linearity of all the equations describing the electromagnetic fields allows us to connect the fields resulting from the scattering process to the incident field through a linear operator that, acting on the incident field, returns the scattered field [5]:

$$\vec{E_S} = \mathbb{S}\vec{E_i}$$

When this operator is represented on the basis of the spherical multipole fields, it is known as the *transition matrix* (T-matrix) and is defined by the equation:

$$A_{l'm'}^{(p')} = \sum_{plm} S_{l'm'lm}^{(p'p)} W_{lm}^{(p)} \tag{8}$$

In this representation, the operator links the amplitudes of the incident field to those of the scattered field. However, the most relevant result of this approach is that the T-matrix, for a given wavelength and after imposing the boundary conditions, depends solely on the chemical and physical properties of the scatterer being independent both from the state of polarization of the incident field and from the scattering geometry of the process [15].

In far-field regime, where the EM field is described by the multipole expansions containing only the transversal components of the field. It is possible to find the

relation between the $\mathbb{S}-matrix$ coefficients and the scattering amplitude that, for a $\eta'-$polarized incident field, is:

$$f_{\eta'\eta} = -\frac{i}{4\pi k_m}\sum_{plm} W_{lm}^{(p)*}(\hat{e}_{s\eta'},\hat{k}_s)A_{lm}^{(p)}(\hat{e}_{i\eta},\hat{k}_i) =$$

$$= -\frac{i}{4\pi k_m}\sum_{plm}\sum_{p'l'm'} W_{lm}^{(p)*}(\hat{e}_{s\eta'},\hat{k}_s)S_{lml'm'}^{(pp')}W_{l'm'}^{(p')*}(\hat{e}_{i\eta},\hat{k}_i) \tag{9}$$

This equation is one of the most important relations in the electromagnetic theory of scattering as it links the measurable physical quantities, such as the cross sections, to the elements of the T-matrix that contain the optical properties of the scatterer. Indeed, applying the optical theorem and assuming that the T-matrix elements are known, we can write the relation between the extinction cross section σ_T and the forward scattering amplitude as follows:

$$\sigma_{T,\eta\eta'} = \frac{4\pi}{k_m} Im[\mathbf{f}_{\eta\eta'}(\hat{k}_s=\hat{k}_i,\hat{k}_i;\hat{e}_i)\cdot\hat{e}_i] =$$

$$= -\frac{1}{k_m^2}\sum_{plm}\sum_{p'l'm'} W_{\eta lm}^{(p)*}S_{lml'm'}^{(pp')}W_{\eta'l'm'}^{(p)*} \tag{10}$$

Moreover, even the scattering cross-section, the ratio of all the energy scattered by the particle to the incident energy, can be expressed in terms of the forward scattering

amplitude:

$$\sigma_{S\eta\eta'} = \int |\mathbf{f}_{\eta\eta'}(\hat{k}_s = \hat{r}, \hat{k}_i; \hat{e}_i) d\Omega =$$

$$= \frac{1}{k_m^2} \sum_{plm} \sum_{p'l'm'} \sum_{p''l''m''} S^{(pp')*}_{lml'm'} W^{(p')*}_{\eta l'm'} S^{(pp'')*}_{lml''m''} W^{(p'')}_{\eta' l''m''} \tag{11}$$

At this stage, it is evident that the knowledge of the T-matrix of the particle concerned has paramount importance for the interpretation of the optical behavior, as it can be directly linked to optical cross sections. At this point our attention shifts to the methodology by which it is possible to determine the elements of the T-matrix $\mathbb{S}$ and consequently, through equation 8, the coefficients of the scattered field.

1.3.4 The case of spherical scatterer

If the particle of interest has a spherical shape the expansion of the field into a series of spherical multipole fields make the imposition of the boundary conditions across the surface of the particles an easy matter because, as far as the spherical particle is radially homogeneous, even the fields within the sphere must be regular at the origin and their expansion can be taken in the form:

$$\vec{E_t}\eta = E_0 \sum_{plm} C^{(p)}_{\eta lm} \vec{J}^{(p)}_{lm}(k_p, \vec{r}) \tag{12}$$

$$i\vec{B} = \frac{1}{k_m} \nabla \times \vec{E} \tag{13}$$

where $k_p = n_p k_0$, n_p being the refractive index of the particle. Now, on account that the transverse harmonics form a complete orthonormal set tangent to the surface of the unit sphere, it is possible to apply the boundary conditions simply by equating the dot products of the internal and the external fields with the transverse harmonics and integrate *analytically* the resulting equations over the solid angle [15].

The result of this procedure yield a system of equations among which the amplitudes of the internal field can be easily eliminated and, in the case of homogeneous sphere, the scattering coefficients are related to the incident coefficients as follows:

$$A^{(p)}_{\eta lm} = -R^{(p)}_l W^{(p)}_{\eta lm} \tag{14}$$

where the quantities $R^{(1)}_l$ and $R^{(2)}_l$ coincide with the well known Mie scattering coefficients, b_l and a_l, respectively [16].

This procedure can be extended also to radially non-homogeneous spheres when the refractive index is space-dependent. In this case, the electric and the magnetic field do not satisfy the Helmholtz equation but rather a system of analogous equations in which the electric and magnetic fields are coupled because of the assumed inhomogeneity of the medium. Due to the spherical symmetry of the scatterer, however, the internal field can still be expanded in a series of multipole fields in which the radial function is no longer Bessel's function but a more general and numerically determinable function that takes into account the radially non-homogeneity of the sphere. In this case is possible to determine once again a relation formally analogous to equation 14, in which now the quantities $R^{(p)}_l$ constitute a set of generalized Mie

coefficients [17].

1.3.5 The case of nonspherical scatterer

The particles that are most commonly met in actual observations are nonspherical and, even when their orientations are randomly distributed, the effects that stem from the lack of sphericity may be attenuated but never fully canceled by the averaging procedure. For these reasons, the possibility to determine the optical properties of these particles has been and still is a crucial question in light scattering theory and simulation. Several attempts have been made to devise model nonspherical particles whose optical properties could be calculated as exactly as possible without resorting to a purely numerical approach like FDTD (finite difference time domain), FEM (Finite element method), or DDA (Discrete-Dipole Approximation). Several attempts have been made to devise model nonspherical particles whose optical properties could be calculated as exactly as possible [18] [19] [20], i.e., without resorting to any approximation. However, one of the most promising procedure devised to simulate a real non-spherical scatterer consists in modeling the real shape by an aggregate of N, not necessarily equal spheres, whose mutual distances are so small that they must be dealt with as one object [21].

In the following, we briefly report the procedure for calculating the T-matrix for a cluster of spheres starting from one of the most useful and important properties of the electromagnetic fields: the principle of superposition.

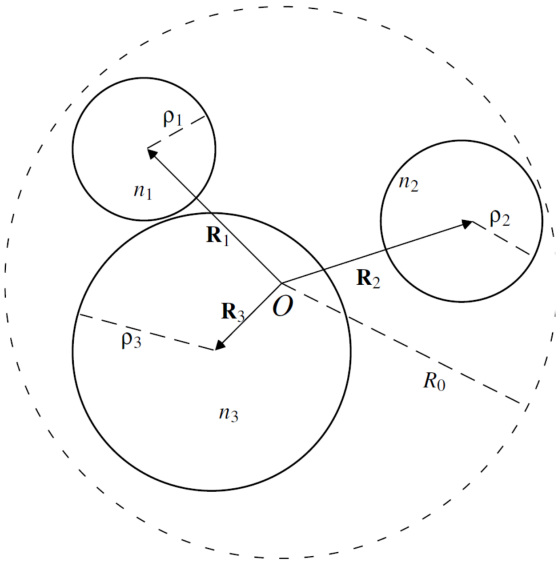

Figure 3: Sketch of a 3-sphere cluster. The dashed curve separates the near from far-field region; in this latter, the optical behavior can be described through the definition of T-matrix. Figure from [15]

Thanks to this property, it is possible to write the field scattered by the whole aggregate as the superposition of the fields scattered by each of the spheres in the form:

$$\vec{E}_{s\eta} = E_{0\eta} \sum_{\alpha} \sum_{plm} \mathcal{A}^{(p)}_{\eta\alpha lm} \vec{H}^{(p)}_{lm}(k_m, \vec{r}_\alpha) \tag{15}$$

where the amplitudes $\mathcal{A}^{(p)}_{\eta\alpha lm}$ should be calculated so that $\vec{E}_{s\eta}$ satisfy the appropriate boundary conditions at the surface of each of the spheres, whose inner field is of the form:

$$\vec{E}_{t\eta\alpha} = E_{0\eta} \sum_{\alpha} \sum_{plm} \mathcal{C}^{(p)}_{\eta\alpha lm} \vec{J}^{(p)}_{lm}(k_p, \vec{r}_\alpha) \tag{16}$$

By analyzing the equation 15, it is possible to note that the scattered field is given by a linear combination of multiple fields that have different origins, whereas the incident field is given by a combination of multipole fields centered at the origin of the coordinates. Since the boundary conditions must be imposed at the surface of each of the spheres, e.g., of the α-sphere, it is necessary to apply the addition theorem for vector spherical harmonics [22] and to rewrite the whole field in terms of multipole fields centered at R_α:

$$\vec{E}_{s\eta} = E_{0\eta} \sum_{plm} [\mathcal{A}^{(p)}_{\eta\alpha lm} \vec{H}^{(p)}_{lm}(k_m, \vec{r}_\alpha) + \sum_{\alpha'} \sum_{p'l'm'} \mathcal{H}^{(pp')}_{\alpha lm,\alpha' l' m'} \mathcal{A}^{(p')}_{\eta\alpha' l' m'} \vec{J}^{(p)}_{lm}(k_m, \vec{r}_\alpha)] \tag{17}$$

where the quantities $\mathcal{H}$ are responsible of the translation of multipole fields from α' sites to α sphere.

After applying the boundary conditions on the surfaces of each of the spheres, it is necessary to apply the addition theorem so as to refer all the quantities to a single origin. At the end, the elements of the T-matrix are:

$$S^{(p,p')}_{lml'm'} = - \sum_{qLMq'L'M'} \sum_{\alpha\alpha'} \mathcal{I}^{(pq)}_{0lm\alpha LM} [M^{-1}]^{(qq')}_{\alpha LM\alpha' L'M'} \mathcal{I}^{(q'p')}_{\alpha' L'M'0l'm'} \tag{18}$$

The T-matrix of the whole aggregate defined above has the correct transformation properties under rotation. In addition, as a consequence of the lack of spherical

symmetry of the aggregate as a whole, is non-diagonal and contains all the multiple scattering contributions due to the interaction among the spheres that form the cluster.

1.4 Dipole Approximation

Rayleigh scattering refers to the study of the phenomenon of light diffusion when the incident wavelength is much larger than the average size of the sample particles. In this case, if r_p is the minimum radius of the sphere containing the scatterer, $x|n_p/n_m| = \frac{2\pi r_p}{\lambda_0}|n_p/n_m| << 1$ and we can model the particle as an induced dipole immersed in an electromagnetic field $\vec{E}(r,t)$, which can be considered homogeneous inside the particle [23] [24].

This last condition is important when considering the applicability of the dipole approximation and has to be considered with care when we deal with high refractive index dielectric particles or metal nano-particles, where the presence of plasmonic resonances dominates the optical response [25]. In the range of validity of this approximation, if the external field is not too large, the induced dipole moment, $\vec{p}(r,t) = \alpha_p \vec{E}(\vec{r},t)$, is proportional to the external field through a linear complex polarisability, α_p, as corrected by Draine and Goodman to satisfy the optical theorem [26]:

$$\alpha_p = \alpha_0(1 - i\frac{2k_m^3\alpha_0}{3\epsilon_m})^{-1}$$

with ϵ_m dielectric permittivity of the medium and α_0 being the static Clausius-Mossotti polarisability,

$$\alpha_0 = 3V\epsilon_m \frac{\epsilon_p - \epsilon_m}{\epsilon_p + 2\epsilon_m}$$

where V is the particle volume and ϵ_p is the dielectric permittivity of the particle.

When the electric dipole $\vec{p}$ is illuminated by a plane electromagnetic wave $\vec{E}_i$ whose intensity is given by $I_i = \frac{1}{2} n_m c |E_i|^2$, the extinction cross-section, defined as the ratio between the power removed from the EM field by the dipole and the incident intensity, is given by:

$$\sigma_e^{(d)} = 4\pi k_0 Im(\alpha_p)$$

Similarly, if we now consider the rate of energy scattered by the particle to the incident intensity, we obtain the scattering cross-section as:

$$\sigma_s^{(d)} = \frac{8\pi k_0^4}{3} |\alpha_p|^2$$

The usefulness of the dipole approximation is to give a simple analytical approach which permits to obtain quantitative information on the optical properties of nanoparticles and, as we can see in the next sections, on the optical trapping (force components, trap stiffness) of small particles in many different beam configurations.

1.5 Numerical Methods

The scattering properties of a particle are intimately related to its physical and geometrical parameters, such as size, shape, refractive index, and orientation. Therefore, understanding the optical phenomena and developing particle characterization techniques require accurate knowledge of the electromagnetic interaction as a function of particle parameters.

Although light scattering by spherical scatterers can be very well described by Lorentz-Mie theory, when one is interested in effects that depend on the precise shape of the particles concerned, the use of more sophisticated methods is in order. Most of the theories belong to one of these two broad categories:

differential equation methods, that compute the scattered field by solving the Maxwell or the vector wave equations in frequency or time domain;

integral equation methods, based on the volume or surface integral counterparts of the Maxwell equations.

Of course, the T-matrix method on which our approach is based is only one of the methods that were devised to study the scattering properties of non-spherical particles. In this respect, the T-matrix method, derived by Waterman [5] starts from the integral equation formulation of electromagnetic scattering from particles. This formulation also called the extended boundary conditions method, relies on integrals over the volume or, more often, over the surface of the particle. Provided

these integrals can be performed with sufficient accuracy, the extended boundary conditions method accounts very well for the actual shape of the particle. A survey of all the methods that have been developed to deal with scattering from particles of general shape has been given by Mishchenko and Travis [4] and by Kahnert [27] .

Here, I report a brief description of the framework of the so-called finite elements methods, of which *Lumerical* constitute a smart implementation, which is in common use for studying electromagnetic scattering from particles of complicated shape. The description does not pretend to be exhaustive and is meant to understand the similarities and differences of the results obtained with different approaches.

1.5.1 Finite Difference Time Domain Method: conceptual basis and diagram of the simulation process

Most of the methods that are in common use for calculating the scattered field from particles seek solutions of the Maxwell equations in the frequency domain. From a mathematical point of view, Maxwell equations in the frequency domain are elliptic so the imposition of the boundary conditions is essential for finding solutions that describe actual wave propagation. On the contrary, the finite difference time domain method (FDTD) is a finite-elements method based on the numerical integration of the Maxwell equations in the time domain [28]. This means that the solution to the scattering problem is dealt with as an initial value problem, and the incident field has not to be a monochromatic wave. In principle, boundary conditions are not necessary because, in the time domain, the Maxwell equations are hyperbolic [29].

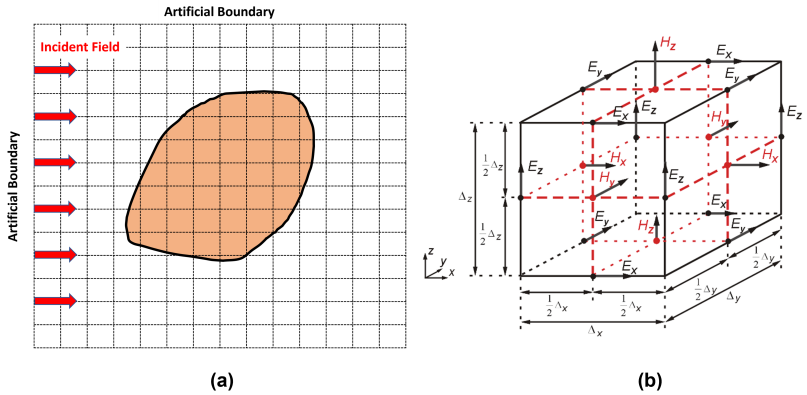

Figure 4: (a) Sketch of the discretized region for the computation of the near-field by the FDTD method; (b) and scheme of field components on a cubic cell. [4]

The FDTD approach is a direct implementation of Maxwell's time-dependent curl equation for the temporal variation of electromagnetic waves within a finite space that contains the scattering object. The electromagnetic properties as functions of the spatial location are specified by defining the permittivity, permeability, and conductivity at each grid point, as shown in the conceptual diagram in figure 4.

The time-dependent Maxwell's curl equations are discretized by using the finite difference approximation in both time and space. At the initial time t = 0, the incident field is turned on and propagates toward the particle. After the interaction, a scattering event is established. The spatial and temporal variations of the electromagnetic field are simulated and computed through time-matching iterations over the entire computational domain, and the information on the convergent scattered field can be obtained when a steady-state field is established at each grid point if a sinusoidal source is used, or when the electric and magnetic fields in the

computational domain have reduced to significantly small values if a pulse source is implemented.

The conventional FDTD numerical algorithm is based on Cartesian grid meshes by defining a regular array of cells whose vertices are commonly referred as *node*. When a scattering particle with a non-rectangular surface is discretized over a Cartesian grid mesh, a staircasing effect occurs that could alter the optical response of the simulated system. For this reason, various FDTD algorithms associated with global curvilinear and obliquely Cartesian grids have been implemented [30] and to economize the computer memory and central processing unit (CPU) time demands, some FDTD algorithms have been introduced to allow a coarse grid size and the subgridding technique [31] [32]. Although the curvilinear grid and target-conforming schemes are more accurate, they are inherently more complicated and tedious than rectangular Cartesian schemes. In addition, it has been shown that the staircasing effect is not a serious problem when the simulations are performed for the computation of light scattering by nonferromagnetic and nonconducting nano/micro nanoparticles once a proper method is developed to evaluate the dielectric constants over the grid points [33]. Although the actual process of scattering of an electromagnetic wave by a particle occurs in unbounded space, the diagram presented in figure 2 shows that in practical applications of the FDTD technique, it is also necessary to introduce artificial boundaries. To meet the demand that the simulation of the field within the truncated region is the same for the unlimited case, an artificial boundary must be imposed with a property known as the *absorbing* or *transmitting* boundary condition. Otherwise, the spurious reflections

off the boundary would alter the near field within the truncated domain. The construction of an efficient absorbing boundary condition is an important aspect of the FDTD technique, as an inappropriate boundary condition may lead to numerical instability, thus requiring more computer memory and CPU time.

As the values of the near field computed by the FDTD finite difference are in the time domain, the frequency response of the scattering particle can be obtained by transforming the field from the time domain to the frequency domain. This procedure is not so straightforward, especially when it is necessary to use a Gaussian pulse as an incident field. An inaccurate choice of the beam parameters could introduce aliasing effects and dispersion phenomena.

Once the near-field simulations are performed, the scattering and extinction cross-section can be obtained by invoking a surface-integration technique [34] [33] associated with the tangential components of electromagnetic fields on a surface enclosing the particle or a volume-integration technique [35].

On the basis of the preceding discussions, the major steps required are the following: (a) discretize the finite space containing the particle by a grid mesh; (b) simulate the field in the region by the finite difference analog of Maxwell's time-dependent curl equations; (c) apply boundary condition to suppress the unwanted reflection from the boundary of the computational domain; (d) transform the near field from the time domain to the frequency domain; (e) transform the near field in the frequency domain to the far field with a suitable electromagnetic integral method.

In the next subsection, the theoretical basis for the formulation of finite difference equations analog to the time-dependent Maxwell's curl equations is presented.

1.5.2 Equations analog of the time-dependent Maxwell's curl equations

As stated above, in the framework of the FDTD approach the electromagnetic wave is simulated in the time domain so that from a mathematical point of view, the interaction is an initial value problem. The well-known time-dependent Maxwell's curl equations are given by

$$\nabla \times \vec{H}(\vec{r},t) - \frac{\epsilon(\vec{r})}{c}\frac{\partial \vec{E}(\vec{r},t)}{\partial t} = 0 \tag{19}$$

$$\nabla \times \vec{E}(\vec{r},t) + \frac{1}{c}\frac{\partial \vec{B}(\vec{r},t)}{\partial t} = 0 \tag{20}$$

where the permeability has been assumed to be unity, ϵ is the permittivity of the dielectric medium, and c is the speed of light in a vacuum. Based on the definition of effective dielectric constants, $\epsilon = \epsilon_r + i\epsilon_i$, Eq. (19) can be expressed conveniently as follows:

$$\nabla \times \vec{H}(\vec{r},t) = \frac{\epsilon_r(\vec{r})}{c}\frac{\partial \vec{E}(\vec{r},t)}{\partial t} + k\epsilon_i(\vec{r})\vec{E}(\vec{r},t) \tag{21}$$

To construct the finite difference analog of Maxwell's equations, the computational space (see Figure 4) containing the scattering particle is discretized by defining a regular array of cells whose vertices, commonly referred to as nodes, are individuated

by three integers such that the vector position of node $(i,\ j,\ k)$ is

$$\vec{r}_{ijk} = i\Delta x\,\vec{\hat{e}}_x + j\Delta y\,\vec{\hat{e}}_y + k\Delta z\,\vec{\hat{e}}_z\ .$$

The particle is then characterized by assigning the value of the dielectric function at each node within the volume occupied by the particle itself. This procedure, which is similar to the one used in the DDA, does not require the particle to be homogeneous or to have a regular shape. Each space- and time-dependent variable, such as the components of the fields, is discretized as

$$F(\vec{r},t) \rightarrow F_{\mathrm{d}}(i,j,k;n) = F(i\Delta x, j\Delta y, k\Delta z; n\Delta t)\ ,$$

and this procedure is used to write the discretized version of the Maxwell curl equations to be integrated numerically. According to Yee's numerical strategy [36], the magnetic field at the center of cell faces and the electric field counterparts at the cell edges are considered (see figure 4) in order to ensure the continuity at the cell interfaces of tangential components of the electric field and normal components of the magnetic field respectively. As an example, from equation 19, the discretized cartesian x-component of the electric field can be written as follows:

$$\begin{aligned} E_x^{n+1}(i,j+1/2,k+1/2) = a(i,j+1/2,k+1/2)E_x^n(i,j+1/2,k+1/2)+ \\ b(i,j+1/2,k+1/2)[\frac{c\Delta t}{\Delta y}(H_z^{n+1/2}(i,j+1,k+1/2) - H_z^{n+1/2}(i,j,k+1/2))+ \\ \frac{c\Delta t}{\Delta z}(H_y^{n+1/2}(i,j+1,k) - H_y^{n+1/2}(i,j+1/2,k+1)] \end{aligned}$$

And, from equations 21, the discretized cartesian x-component of the magnetic field is:

$$H_x^{n+1}(i+1/2,j,k) = H_x^{n-1/2}(i+1/2,j,k)+$$
$$[\frac{c\Delta t}{\Delta y}(E_z^n(i+1/2,j-1/2,k) - E_z^n(i+1/2,j+1/2,k))+$$
$$\frac{c\Delta t}{\Delta z}(E_y^n(i+1/2,j,k+1/2) - E_y^n(i+1/2,j,k-1/2))]$$

From the preceding equations, it can be seen that the E and H fields are interlaced both in time and in space. Provided that the initial values of the electric and magnetic fields are given, these expressions are suitable for a time-marching iteration procedure. The propagation of the wave can then be simulated by updating the E and H fields in a straightforward manner without imposing the electromagnetic boundary condition at the particle surface. In practice, given the field at t = 0, one is confronted with the numerical integration of a system of six coupled finite-difference equations for the space-time propagation of the field. Six schemes of integration have been devised, each of which is applicable to one of the six rules that are used to approximate the derivatives of the field components. Without dwelling on the technical definition of these rules, suffice it to say that three of them refer to first discretizing the temporal derivatives, and the others three refer to first discretize the spatial derivatives. More details on this argument can be found in the specific scientific literature. Here it is possible to state that the spatial discretization scheme and the temporal discretization scheme, when compared to Lorenz–Mie solution, produce the same, while different, grid-size dependent accuracy for the computed phase functions. Once a scheme is selected, one gets the near field within the whole

region of integration as a function of time.

The FDTD technique is then simple in concept and also efficient in numerical computations, however, the actual situation is more complicated than stated above.

First, in order to ensure the stability of the numerical integration of the Maxwell equations, the space and time increments must satisfy the condition [37]

$$c\Delta t \leq \left[1/(\Delta x)^2 + 1/(\Delta y)^2 + 1/(\Delta z)^2\right]^{-1/2}$$

that sets a lower limit to the number of nodes that are necessary to get reliable results.

Second, any scattering process occurs in infinite space, whereas, for evident computational reasons, the integration of the discretized Maxwell equations must be performed within a finite region. It is, therefore, necessary to introduce appropriate boundary conditions across the surface, which limits the region of integration to prevent unphysical reflections of the field that would otherwise modify, even severely, the near field [38] [39].

Of course, the field calculated as outlined above is the near field, whereas to calculate the quantities of interest, such as the cross sections, one needs the far field. This task is faced by means of Green's second vector identity that ensures the matching of the near and the far-field through integration on any suitable surface containing the particle [34] [35].

Finally, let us recall that since the incident field is, in general, non-monochromatic, also the far field is non-monochromatic. Therefore, in order to get the frequency response of the particle one has to resort to a discrete Fourier transform so that the results of the FDTD method can be compared with those of more conventional methods that yield the field in the frequency domain. The results of such comparisons prove that the FDTD method achieves extremely good precision in the calculation of the fields [4].

Chapter 2

Theory of optical forces and optical tweezers

A fundamental aspect of the interaction between electromagnetic radiation and matter concerns the laws of conservation of energy, linear and angular momentum. As a consequence of the conservation of linear momentum, for example, light has the ability to exert a force on the matter. The first to notice such mechanical effects was probably Kepler, in 1619, noting that the direction of the tail of comets along their path around the Sun is also due to the pressure of solar radiation exerted on the particles that make it up. It was Maxwell, in 1873, who theoretically deduced this optical effect. And Lebedev, Nichols, and Hull were the physicist who made the first experimental measurements in 1901.

2.1 Conservation laws, Maxwell stress tensor, radiation force and torque

2.1.1 General Remarks

In any experimental condition or theoretical approximation, the interaction between matter and EM radiation is subject to the three laws of conservation: energy, linear momentum, and angular momentum [10]. In particular, the conservation of the

linear momentum, stated for the combined system of field and particles, plays a fundamental role in determining the dynamical behavior of the nano-particles through the radiation force $\vec{F}_{rad}$ [10] [15]; on the other hand, the angular momentum conservation has an important role in the manipulation of small particles under controlled laboratory conditions and is responsible for their partial alignment due to radiation torque $\vec{T}_{rad}$ [10] [15].

When a monochromatic light impinges on a particle, the time-averaged optical force and torque exerted on the object are given by:

$$\vec{F}_{rad} = \oint_S < \mathrm{T_M} > \cdot \hat{n} dS \tag{22}$$

$$\vec{T}_{rad} = \oint_S (< \mathrm{T_M} > \times \vec{r}) \cdot \hat{n} dS \tag{23}$$

where the Gaussian units used and the integration is conducted over the surface S surrounding the scattering particle, $\hat{n}$ is the outward normal unit vector, $\vec{r}$ is the vector position, and $< \mathrm{T_M} >$, the time-averaged Maxwell stress tensor describes the mechanical interaction of light with matter. For our purposes, always considering harmonic fields at angular frequency ω in a homogeneous, linear, and non-dispersive medium, the averaged Maxwell stress tensor is [40]:

$$\mathrm{T_M} = \frac{1}{8\pi} Re \left[\vec{E}_{tot} \otimes \vec{E}_{tot} + \vec{B}_{tot} \otimes \vec{B}_{tot} - \frac{1}{2} (\vec{E}_{tot} \cdot \vec{E}_{tot} + c^2 \vec{B}_{tot} \cdot \vec{B}_{tot}) \mathrm{I} \right]$$

where $\vec{E}_{tot} = \vec{E}_i + \vec{E}_s$, $\vec{B}_{tot} = \vec{B}_i + \vec{B}_s$, $\otimes$ represents the dyadic product and I is the dyadic unit.

These expressions for optical force and torque can be simplified by integrating the Maxwell stress tensor over a spherical surface of radius R which contains the particle and considering the properties of the fields in the far zone. In fact, far from the particle, the fields are transverse and the dyadic terms in the Maxwell stress tensor vanishes. In this way, the resulting optical force components along a direction characterized by the unit vector $\hat{u}_\zeta$ is given by:

$$\vec{F}_{rad\zeta} = -\frac{-r^2}{16\pi} Re \int_\Omega (\hat{r} \cdot \hat{u}_\zeta)[n_m^2(|E_s|^2 + 2\vec{E}_i^* \cdot \vec{E}_s]) + (|B_s|^2 + 2\vec{B}_i^* \cdot \vec{B}_s])]d\Omega \quad (24)$$

The calculus of torque requires a well-established origin, so we choose a frame of reference with the origin within the particle concerned. Since the dynamics of any body is determined by its center of mass and by its principal axes of inertia, choosing this particular set of axes as a frame of reference would greatly simplify the study of the dynamics. The integration surface can then be chosen to be a large sphere with a center at the origin, and we can write:

$$\vec{T}_{rad} = -\frac{-r^3}{8\pi} Re \int [\hat{r} \cdot (\vec{E}_i + \vec{E}_s)(\vec{E}_i^* + \vec{E}_s^*) \times \hat{r} + \hat{r} \cdot (\vec{B}_i + \vec{B}_s)(\vec{B}_i^* + \vec{B}_s^*) \times \hat{r}]d\Omega \quad (25)$$

Note that for radiation torque, the far field expression of the scattered fields cannot be used as they are orthogonal to the radial unit vector $\hat{r}$, thus providing a vanishing result. In the following sections, for a correct calculation of the radiation torque, one

has to retain the *radial terms of the fields*, which for the case of the radiation forces, have been neglected because they vanish faster than $1/r$.

2.2 Optical Forces in T-matrix formulation

Starting from equation 24 and after some substitutions and mathematical steps, Mishchenko et al. [41] provided the force originated from the scattering process of a linear polarised plane wave by a spherical homogeneous particle through the following equation:

$$\vec{F}_{rad} = \frac{n_m}{c} I_0 \left[\sigma_e \hat{k_I} - \int_\Omega \frac{d\sigma_s}{d\Omega} \hat{r} d\Omega \right] \tag{26}$$

This relation shows some interesting features as it elegantly links the radiation force to measurable optical quantities such as the extinction cross-section, forward scattering information, and the differential scattering cross-section containing information on the anisotropy of the particle through the asymmetry parameter [42].

On the other hand, when we deal with scatterers more complex than the single homogeneous sphere, such as radially symmetric non-homogeneous scatterers or cluster, the expression of the radiation force should be rewritten in terms of the T-matrix. By developing the fields involved in the relationships 26 in terms of spherical vector multipoles, the components along the coordinator axis (ζ), it is found that the radiation force can be written as the sum of two components [42][43]:

$$F_{rad\zeta} = -F_{rad\zeta}^{(sca)} + F_{rad\zeta}^{(ext)} \tag{27}$$

where

$$F_{rad\zeta}^{(sca)} = \frac{\epsilon_m E_i^2}{2k_m^2} Re\left[\sum_{plm}\sum_{p'l'm'} A_{lm}^{(p)*} A_{l'm'}^{(p')} i^{l-l'} I_{lml'm'}^{(pp')}\right] \tag{28}$$

$$F_{rad\zeta}^{(ext)} = -\frac{\epsilon_m E_i^2}{2k_m^2} Re\left[\sum_{plm}\sum_{p'l'm'} W_{lm}^{(p)*} A_{l'm'}^{(p')} i^{l-l'} I_{lml'm'}^{(pp')}\right] \tag{29}$$

where E_i is the amplitude of the incident field, and:

$$I_{lml'm'}^{(pp')}(\hat{u}) = \int_\Omega (\hat{r}\cdot\hat{u}) i^{p-p'} \vec{Z}_{lm}^{(p)*}(\hat{r}) \cdot \vec{Z}_{l'm'}^{(p')}(\hat{r}) d\Omega$$

are matrix elements that, thanks to the orthogonal properties of the spherical harmonics, can be calculated analytically.

We first note that in the preceding relations (27-29) the fictitious dependence on the radius of the integrating sphere does not appear. Then we highlight that the first component of the force depends exclusively on the coefficients of the scattered field, while the second also depends on those of the incident field, just like the scattering and extinction sections, hence the definition F_{scat} and F_{ext}.

Another point to note is that these relationships remain valid even if the incident field is an overlap of plane waves. This consideration will be useful in the analysis of the optical tweezer system.

2.2.1 Modeling the electromagnetic focused field in T-matrix approach

One of the strong points of the T-matrix formalism is its applicability to any field that can be described as overlapping plane waves. Even an electromagnetic field due to a laser beam focalized by an aplanatic lens can be written in these terms resorting to the *representation of angular spectrum* [44]. To this end, we consider a lens of focal length f with numerical aperture NA where n_m is the refractive index of the medium that fills the image space field. According to Novotny and Hecht [45], the field at any point within the focal region can be written using the angular spectrum representation as:

$$\vec{E}(\vec{r}) = \int_{k_x^2+k_y^2 \leq k_\perp^2} E_{PW}(\hat{k}) \hat{u}_{\hat{k}} e^{i\vec{k}\cdot\vec{r}} dk_x dk_y \tag{30}$$

where the limits of integration ensure that only the rays that traverse the exit pupil of the optical system are considered and E_{PW} is a quantity related to the focal length and to the apodization function that gives the profile of not only TEM_{00} but also of higher Gaussian modes TEM_{10} and TEM_{01}. This representation can be extended to the case of an image space not filled by a single homogeneous medium but rather by two homogeneous media of different refractive indexes, separated by a plane interface orthogonal to the optical axis, thus introducing aberration effects that should, in principle, be considered and that represent the actual situation used in optical tweezers [46] [47] [1]. In figure 5, we report the angular spectrum representation for a focused TEM_{00} Gaussian x-polarized beam obtained by focusing the incident field at λ=830 nm through a lens with NA=1.3.

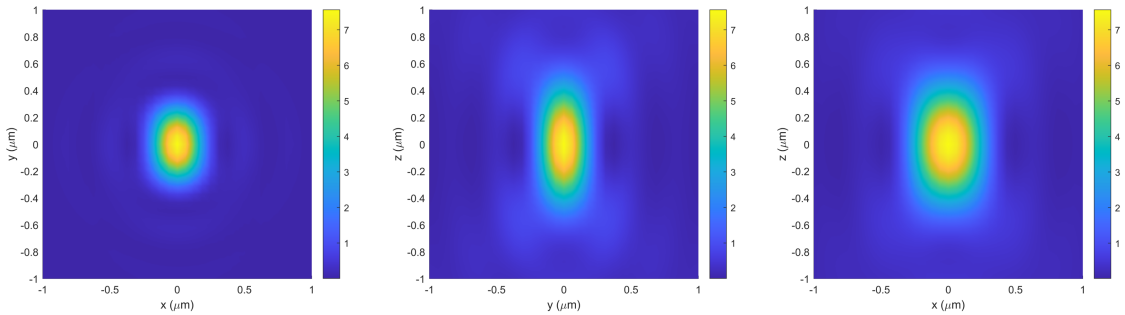

Figure 5: Angular spectrum representation of intensity for a TEM_{00} Gaussian x-polarized beam. In panel (a), the map is for the normalized intensity in x-y plane (perpendicular to the optical axis); (b) and (c) are the maps for the normalized intensity in z-y and z-x plane, respectively. The wavelength is 830 nm, the numerical aperture of the lens is 1.3, and the refractive index of the external medium is water

Once we have introduced the T-matrix approach to electromagnetic theory and the representation of angular spectrum to model a focused field, we have all the tools to study the behavior of an optical tweezer formally. In the following chapters, we will introduce some particular systems where we can apply this formalism and appreciate its power and flexibility.

2.2.2 Implementation of computing code

In order to understand the advantages and disadvantages of the various theoretical and numerical approaches aimed at calculating the optical forces, it is necessary at this stage to spend a few words on the architecture of the software that, in the case of the T-matrix approach, is realized using FORTRAN95 high-level programming language. As discussed before, the optical forces in T-matrix formalism can be computed by calculating the amplitudes of multipole expansions that represent

the incident and the scattered fields, see equations 29 and 28. To this end, we have realized two numeric calculation codes, one that determines the amplitudes of the highly focused incident field and the other that, once we have established the properties of the scatterer, provides the amplitudes of the scattered field. These amplitudes, which are recorded on two different service files, are then processed by another code that provides the radiation force values at any point in the grid, combining them according to the equations 29 and 28. This kind of code modularity was chosen to optimize both the resources needed to perform the computation in terms of processing speed and CPU use and the physical space for data storage.

The first code realizes the angular spectrum representation of the incident field determining the multipole amplitudes at the points of intersection of a three-dimensional grid in the focal region, the spacing of which is chosen appropriately to provide a description with the desired resolution. The number of multipole amplitudes thus obtained is a function of the L-value chosen for the truncation of the series expansions that ensures the desired convergence of the calculus. They also depend on the wavelength of the incident radiation, the numerical aperture (NA) of the focusing lens, the *filling factor*, and the value of the dielectric constant of the medium in which the particles are trapped. The influence of the filling factor on the sharpness of the focus affects mostly the effects polarization of the incident field. In fact, from 5 can be noted that the focal region in zy plane and zx plane have different spatial widths. This part of the code is the one that requires most of the processing time, depending on how many points are used for the description of the grid. An increased amount of RAM memory is due to the number of plane waves needed for the

accurate description of the focused field and the truncation value of the multipole expansion. Typically, on an INTEL-coreI7 workstation, if we chose a truncation value L=8, a 3D grid consisting of 51x51x51 points that use for the description of 100 plane waves, the multipolar amplitudes of the incident field can be obtained in a time of about 6 hours, using about 1.5 Gbyte of RAM memory, with a hard disk occupation of about 700 Mbyte. Although these performance parameters may seem rather time and CPU-demanding, it must be considered that once the characteristics of the optical trap have been defined (wavelength, polarization, refractive index of the external medium, ...), the results obtained for the definition of the incident field have a validity that does not depend on the type of particle that the radiation will be able to manipulate. Ultimately, the set of multipolar amplitudes of the incident field thus obtained constitutes a kind of database that can be recalled and used whenever the optical trap has those given characteristics.

The second code, based on T-matrix approaches, computes not only the cross-section of the scatterer for that given wavelength but stores in another service file all the scattering amplitudes, whose number depends on the L-value chosen for the truncation of the series expansion. In most cases, the running time and memory requirement of this code is very short and depends on the complexity of the scatterer whose properties you want to study. Typically, on a INTEL-coreI7 workstation, if we choose a truncation value L=8 that corresponds to study particles with size parameter <5, for a sphere, even stratified, the results are obtained within a few seconds while, for a cluster composed of no more than 10 spheres, the time spent is less than 3 minutes.

Therefore, when it is necessary to carry out several simulations in which the geometries and the composition of the scatterer are modified, for a given type of optical trap, the code based on the T-matrix approach has excellent reliability [15], great versatility and excellent performance in terms of computing time and CPU resources.

2.3 Optical Forces in Dipole Approximation

It can be shown that the optical forces in such a system can be written in the form of [10]:

$$\vec{F}_{DA} = \frac{1}{4} Re\{\alpha_p\} \nabla |E_i|^2 + \frac{\sigma_{ext}}{c} \vec{S}_i - \frac{1}{2} \sigma_{ext} c \nabla \times \vec{s}_d$$

where:

$$\vec{S}_i = \frac{c}{8\pi} Re\{\vec{E}_i \times \vec{B}_i^*\}$$

$$\vec{s}_d = i \frac{1}{8\pi\omega} \vec{E}_i \times \vec{E}_i^*$$

are the time average of the Poynting vector and the time average of the spin density of the incident wave. Each of the three parts that make up the equation has particular characteristics:

- Gradient force: depends on the intensity of the field and is a conservative force. It causes the body to move towards or away from the areas of greatest intensity, depending on whether its polarizability is positive or negative. It can be written in terms of the intensity of the electric field as follows:

$$\vec{F}_{DA}^{G} = \frac{1}{2} Re\{\alpha_p\} \nabla I(r) \tag{31}$$

  being $I(r) = \frac{1}{2} n_m c |\vec{E}(\vec{r})|^2$.

- Scattering force: depends on the Poynting vector relative to the incident radiation and has the same direction; it is a non-conservative force. It's caused

by the processes of transferring the moment of the field to the body, in fact, it is also proportional to the extinction cross-section:

$$\vec{F}_{DA}^{S} = \frac{n_m}{c}\sigma_e I(r) \tag{32}$$

- Spin-curl force: this is also a non-conservative force and stems from the polarization gradient in the incident field.

In the following, we will explicitly formulate the scattering and gradient force due to interaction with a laser beam.

2.3.1 Modeling the electromagnetic focused field in dipole approximation

Consider an incident laser beam with a typical Gaussian intensity profile that propagates along the z-axis [15] as in figure 6, in *paraxial approximation*, that is when all rays entering or leaving a centered optical system propagate from the object plane to the image plane remaining confined in a region close to the optical axis, the complex electric field is represented by:

$$\vec{E}_i(\rho, z) = \vec{E}_0 \frac{\omega_0}{\omega(z)} e^{-\frac{\rho^2}{\omega(z)^2}} e^{i\Phi(z)}$$

where ρ is the radial coordinate, $\vec{E}_0$ is a vector in x-y plan specifying the amplitude, phase, and polarization of the beam, ω_0 is the waist radius, $w(z) = \omega_0\sqrt{1+\frac{z^2}{z_0^2}}$ is

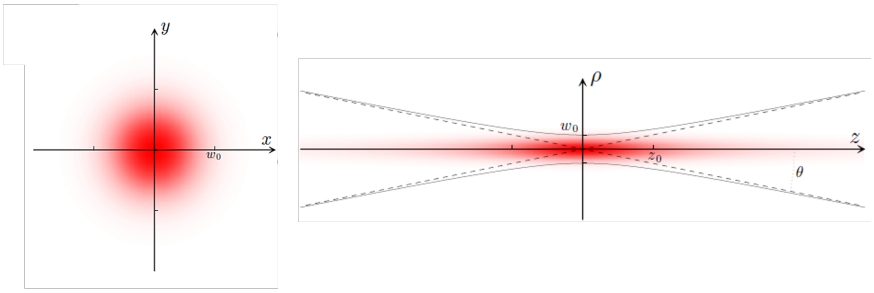

Figure 6: Intensity profile of a Gaussian beam (a) in x,y plane perpendicular to optical axis; (b) along optical axis. [1]

the beam width, where z_0 is the Rayleigh range which denotes the distance from the beam waist at z = 0 to where the beam width increases by a factor $\sqrt{2}$.

The phase $\Phi(z)$ that enters in the second exponential factor depends on the wavefront radius and on the phase correction that happens as the beam propagates through its focus [1]. The intensity of the beam is then:

$$I(\rho, z) = \frac{1}{2} n_m c |\vec{E}(\vec{r})|^2 = I_0 \frac{\omega_0^2}{\omega(z)} e^{-\frac{2\rho^2}{\omega(z)^2}}$$

From equation 31 we can determine the x, y, and z components of the gradient force, which have the following expressions:

$$F^G_{DA,x}(x,0,0) = \frac{2\pi n_m}{c\epsilon_m} Re(\alpha_0) I_0 \frac{\omega_0^2}{\omega^2} (\frac{-4x}{\omega^2}) e^{-2\frac{x^2}{\omega^2}}$$

$$F^G_{DA,y}(0,y,0) = \frac{2\pi n_m}{c\epsilon_m} Re(\alpha_0) I_0 \frac{\omega_0^2}{\omega^2} (\frac{-4y}{\omega^2}) e^{-2\frac{y^2}{\omega^2}}$$

$$F^G_{DA,z}(0,0,z) = \frac{4\pi n_m}{c\epsilon_m} Re(\alpha_0) I_0 \frac{\omega_0^4}{\omega^4 z R^2}(z - z_0)$$

2.3.2 Implementation of computing code

The fully analytical approach offered by the dipole approximation theory (DA) allows the calculation of optical forces by using simple numerical calculation scripts on a programming platform that uses high-level languages. The simulations in dipole approximation that will be presented in the following were carried out using the Matlab programming environment, and, as long as the size parameter $x = k_m a = \frac{2\pi n_m}{\lambda_0} a << 1$ to ensure the validity of DA approach, the numerical estimates of optical forces and trap stiffness can be considered reliable.

In this regard, to have an immediate view on the error that is introduced when the DA approach loses its validity, we report in figure 7 the trap stiffness, that is, the slope of trapping force, calculated along the optical axes in the focal point as a function of the radius a for a dielectric sphere. The curve obtained in DA (dotted line) deviates significantly from that obtained by applying the full scattering theory based on the T-matrix approach (solid red line).

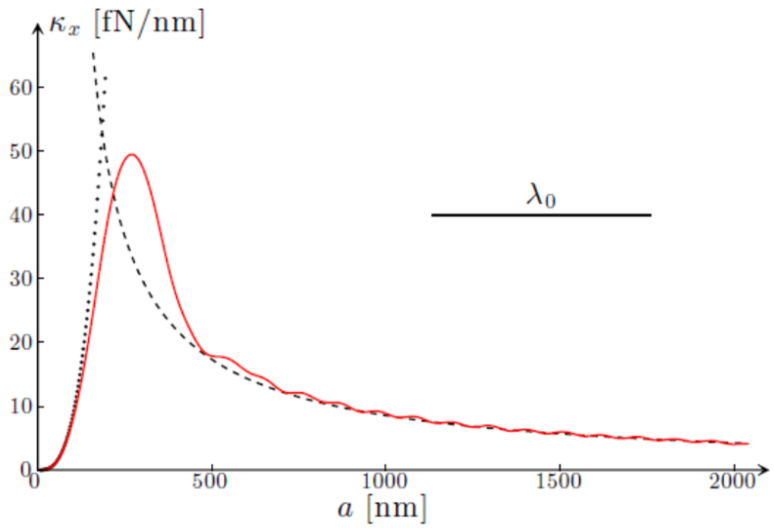

Figure 7: Trap stiffness along optical axes produced by a 10 mW laser beam of wavelength $\lambda = 632$ nm focused by a 1.2 NA objective on a dielectric sphere of radius a ($n_p = 1.50$) in water. The solid line represents the exact electromagnetic calculation. The dipole approximation (dotted line) works for small spheres ($a << 1$). The geometrical optics approximation (dashed line) works for large spheres ($a >> 1$). Figure from [1]

2.4 Optical Forces in Finite Difference Time Domain

The computation of optical forces exerted on a nano-structure by the electromagnetic field realized in the FDTD scheme follows two different approaches: the integration of Maxwell stress tensor over a closed surface and the volumetric technique.

2.4.1 Maxwell Stress Tensor technique

In section 2.1, it has been shown that the conservation laws determine the dynamical behavior of nano-particles so that the time-averaged force F on a particle due to harmonic fields, see equation 23, can be calculated from the Maxwell Stress Tensor, and the net force can be found by integrating numerically this quantity over a closed surface surrounding the particle. In Lumerical implementation for the calculus of this force, it is possible to choose a 2D simulation or a 3D simulation, activating 1D monitors and 2D monitors, respectively, in this way is possible to record the fields on this surface.

The tool to calculate the force is named $tweezer.fsp$, which contains an analysis group named $optical - force - 2D$. The analysis group contains four identical subgroups whose analysis scripts calculate the components of the stress tensor from the simulation. The analysis script of the main group integrates the stress tensor to provide the total force on the particle.

2.4.2 Volumetric technique

The starting point of this approach is to consider that the force on a charged particle in the presence of an electric and magnetic field is given by Lorentz's equation:

$$\vec{F} = q\vec{E} + q\vec{v} \times \vec{B}$$

where q, $\vec{v}$, $\vec{E}$, and $\vec{B}$ are, respectively, the charge, velocity, electric field, and magnetic field.

In a medium with charge per unit volume and current density, the force per unit volume is given by

$$\vec{F_V} = \rho\vec{E} + \rho\vec{J} \times \vec{B}$$

where ρ is the total charge per unit volume and $\vec{J}$ is the total current density. From Maxwell's equations, these quantities are given by

$$\rho = \epsilon_0 \nabla \cdot \vec{E}$$

$$\vec{J} = -\frac{\partial \vec{P}}{\partial t}$$

where $\vec{P}$ is the polarization vector.

In Lumerical's FDTD solver, all the material properties are included in the permittivity. As a result, there is no free current density and no free charge, therefore using a relative permittivity equal to 1 and a free current density of $\vec{J} = \sigma\vec{E}$, in the

frequency domain and with Lumerical's sign convention of $\vec{P}(\omega) = \int e^{i\omega t}\vec{P}(t)$, we have $\vec{J}(\omega) = -i\omega\vec{P}(\omega)$. Due to the preceding relations, the total force per unit volume exerted on the material, in the background with relative permittivity ϵ_b is (note that Lumerical uses SI units):

$$\vec{F_v} = \epsilon_0\epsilon_b(\nabla\cdot\vec{E})\vec{E} - i\omega\vec{P}\times\vec{B} = \epsilon_b\epsilon_0(\nabla\cdot\vec{E})\vec{E} - i\omega\epsilon_0(\epsilon_r - \epsilon_b)\vec{E}\times\vec{B}$$

ϵ_r being relative permittivity.

As reported in the technical notes of Lumerical software, the two techniques give the same result within numerical error, but each has its own strengths and weaknesses. Here we report the key issues of strengths and weaknesses:

Memory: the MST technique requires less memory because it only collects field data on the surface of the box.

Numerical noise: The Volumetric technique is less sensitive to numerical noise, making it the better choice when the force is very small (small index contrast, very tiny particles).

Mesh: The Volumetric technique is sensitive to the number of mesh points. The results become less reliable if the mesh is too coarse.

2.4.3 Modeling the electromagnetic focused field in FDTD

A focused electromagnetic Gaussian beam is modeled starting from the description of a plane wave source. Plane waves are used to inject laterally-uniform electromagnetic energy from one side of the source region. In two-dimensional simulations, the plane wave source injects along a line, while in three-dimensional simulations, the plane wave source injects along a plane (see figure 8 for the geometry). It is also possible to inject a plane wave at a chosen angle.

The plane wave source is actually the same object as the Gaussian source, with the only difference being the source shape settings. By default, the Gaussian sources use a scalar beam approximation for the electric field, which is valid as long as the waist beam diameter is much larger than the diffraction limit. The scalar approximation assumes that the fields in the direction of propagation are zero. For a highly focused beam, there is also a thin lens source that will inject a fully vectorial beam. The cross-section of this beam will be a *Gaussian* if the lens is not filled and will be a *Sinc* function if the lens is filled. In each case, the beams are injected along a line perpendicular to the propagation direction and are clipped at the edges of the source. For uniform illumination (filled lens), the field distribution is precisely the same as described in Mansuripur's papers [48], [49], [50].

As stated in these papers, it must be noted that in non-uniform illumination at a very high numerical aperture, there are some subtle differences depending on whether the incident beam is a Gaussian in real space or in k-space. This difference

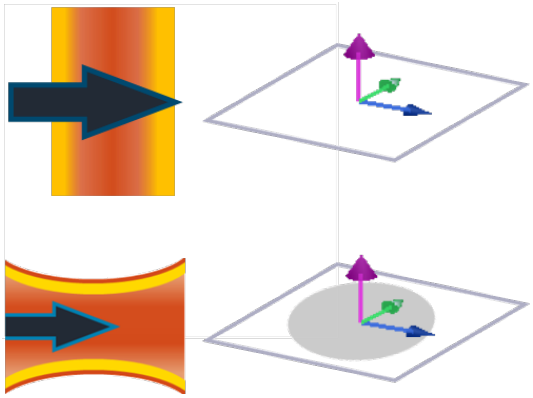

Figure 8: Sketch of the geometry of incident plane wave (upper) and of the Gaussian beam (lower)

is rarely of any practical importance because other factors, such as the non-ideal lens properties, become important at these very high numerical aperture systems.

2.4.4 Implementation of computing code

The implementation of the FDTD approach used in the Lumerical software package provides a powerful tool for understanding the complex interaction between light and matter, including the calculation of optical forces. These simulations can help researchers design and optimize optical systems for various applications, from optical trapping and manipulation to biomedical imaging and sensing. The principal advantages of this implementation are: accuracy, efficiency, flexibility, and the availability of a built-in visualization tool.

- Flexibility: Lumerical simulations are flexible and can be used to model various optical systems, from simple two-dimensional structures to complex three-dimensional systems with multiple materials and geometries. This makes it an

ideal tool for designing and optimizing optical traps and other nanophotonic devices.

- Accuracy: Lumerical simulations are highly accurate, as they directly solve Maxwell's equations without simplifying assumptions. It means that FDTD can capture complex phenomena such as scattering, diffraction, and interference, which are challenging to model using other methods.

- Efficiency: Lumerical simulations are computationally efficient, as they only require the discretization of the electromagnetic fields and the application of finite-difference approximations. This makes it possible to simulate large-scale systems with high accuracy and without requiring extensive computational resources.

- Visualization: Lumerical simulations provide a powerful visualization tool for understanding the behavior of light in optical systems. By visualizing the electric and magnetic fields at each point in the system, it is possible to gain insight into the physical mechanisms underlying the optical forces and optimize their designs accordingly.

In Lumerical, the calculation of optical forces on a spherical model involves several steps:

1. Set up the simulation geometry: this involves defining the size and shape of the simulation region, as well as the properties of the materials in the simulation, such as the refractive index and absorption coefficient. In our calculation, we used a

3D FDTD simulation region that, in all cases, was not larger than 1 micron. For this region it is then necessary to define a coarse mesh grid on the sides of which the fields will be calculated. At this level is necessary to specify also the boundary conditions, which can be either periodic or non-periodic. For non-periodic boundaries, as in the present case, we use the Perfectly Matched Layers (PML) boundary condition that absorb the electromagnetic waves and prevent reflections from the boundaries.

2. Define the incident wave: this step is required to establish the polarization, wavelength, and power of the incident wave. In the present simulations, we use the Gaussian source, which also requires the definition of the Numerical Aperture of the focusing lens, distance from focus, and the power of the incident wave.

3. Create the model: in our case, we considered spheres, so we used the models already present in the libraries of Lumerical. To define the model, we define the size and position of the sphere, as well as its optical properties. The optical properties of the sphere can be specified using its refractive index and absorption coefficient. To obtain an accurate description of the optical forces exerted on the nanostructure, it is necessary to narrow the calculation grid at the position of the scatterer. For this reason, the software gives the possibility to define a fine-mesh grid by varying the spacing between the calculation points.

4. Run the simulation: once the simulation geometry and properties have been defined, the FDTD simulation is run in Lumerical, establishing the number of points at which to perform the simulation. During the simulation, the electric and magnetic fields at each point in the simulation region are calculated iteratively. These fields are

used to calculate the optical forces acting on the spherical model through a built-in application that gives us the possibility to calculate them through the Maxwell stress tensor or through the volumetric technique. In every case, we used the volumetric technique.

Chapter 3

Numerical comparison on representative case studies

In this chapter we present some significant results concerning the comparison between the analytical and numerical approaches aimed to simulate the radiation force acting on nano-structures. In the simulations, the wavelength of the incident field is λ=830 nm and, as an external medium where nano-structures can be trapped, we choose water, with refractive index n_m=1.33, or air, with refractive index n_m=1. Several cases were considered for the purpose of comparison, including:

- Spherical nano-particles with two different radii: 5 nm and 50 nm, made of polystyrene (n_p=1.57), in air.
- Spherical nano-particle with r_p=100 nm, in water, made of a) silica (n_p=2.4), representative of a scatterer with higher optical contrast, and b) polystyrene (n_p=1.57) representative of a scatterer with low optical contrast.
- Dimer: made of two spheres with a radius of 100 nm made of silica (n_p=2.4) immersed in water in two different orientations, representative of a non-spherical scatterer with higher optical contrast.

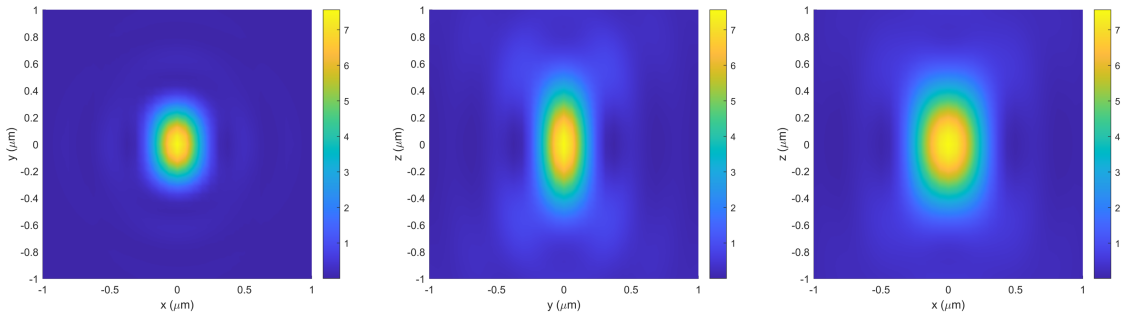

Figure 9: Intensity maps for the incident focalized Gaussian TEM_{00} beam as calculated in the T-matrix formalism. The external medium is water.

3.1 Numerical results for the focused incident field

First of all, in figures 9 and 11 (left) and figures 10 and 11 (right), we report the normalized intensity maps and field profiles where we consider as external medium, in the first case, water ($n_m = 1.33$), and in the second case, air.

It is necessary at this point to note that, despite the good general agreement between the three different methodologies in the description of the incident-focused field, there are some important differences that, in principle, can affect both the determination of the trapping position and the calculation of trap constants, physical quantities that usually are compared with data taken from a real experiment of optical tweezers.

For the angular spectrum representation, we chose, in any case, the *filling factor f*, that is, the rate between the beam waist radius and the aperture radius of the lens, equal to 2. For figures 9 and 11 (left), NA=1.3 while for figures 10 and 11 (right), NA=0.9. To better compare the results for radiation force, in Lumerical simulation,

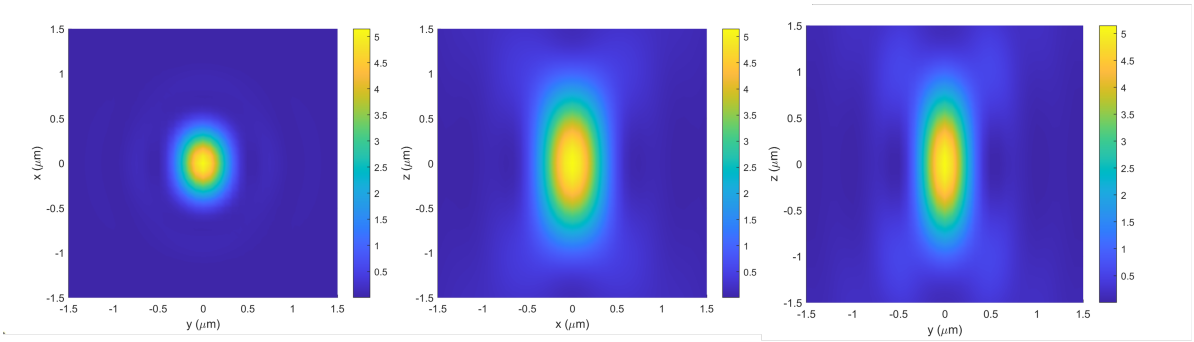

Figure 10: Intensity maps for the incident focalized Gaussian TEM_{00} beam as calculated in the T-matrix formalism. The propagating external medium is air.

this choice corresponds to assume a *filling factor* f=1.875 corresponding to a beam waist radius $\omega_0 = 0.51\frac{\lambda_0}{NA}$, the same parameter that enters in the definition of the incident focalized field as presented in section 2.3.1.

The first question concerns the dependence of the distribution of field intensities on the polarization of the electromagnetic field. By comparing the field maps on the zx plane with that obtained on the zy plane in figure 5, we notice that the polarization dependence is evident as far as we use the angular spectrum representation. In fact, depending on the value of the *filling factor*, as far as it increases, the field confinement increases as well at the focus of the focal spot, becoming more and more elliptical. When the incident field is computed through equations reported in section 2.3.1 (in the paraxial limit), the spot is perfectly circular while a strongly focused beam has a spot that is elongated in the direction of polarization. For this reason, in a typical optical trapping experiment, in which it is necessary to have higher spatially confined light, we need to take into account the vector nature of the fields as it is properly done by the angular spectrum representation as implemented

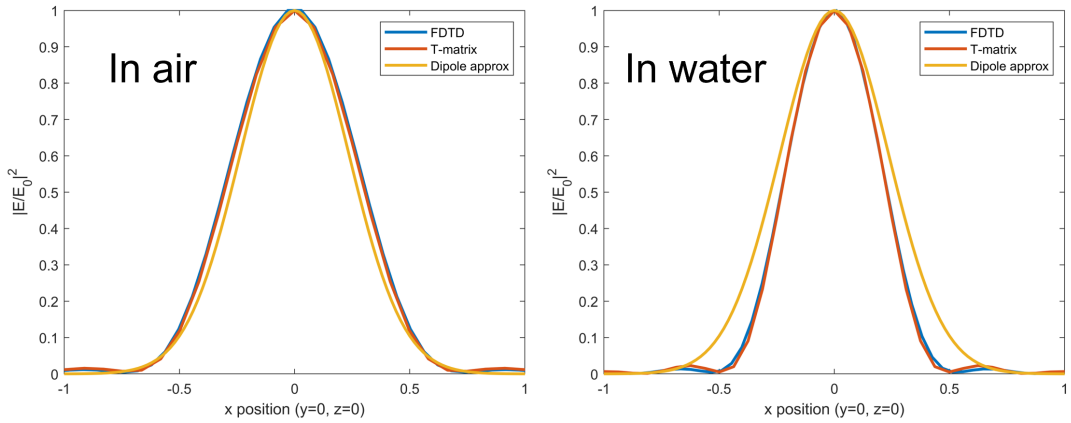

Figure 11: Normalized Intensity profile for the incident focalized Gaussian TEM_{00} beam as calculated in the T-matrix formalism, FDTD approach as implemented in Lumerical and Dipole Approximation. On the left, the propagating external medium is air, and the profiles are computed in the focal region along x, for y=0 and z=0; the same on the right but for water.

in the T-matrix approach. The lack of this characteristic, linked to the nature of the electromagnetic field, while it may not have important consequences as regards the possibility of trapping and manipulation of nano-structures, on the other hand, significantly alters the dynamic behavior of non-homogeneous and/or elongated nano-structures that can rotate possibly aligning with the direction of polarization of the field [51] [40].

The other issue is related to the extension of the focal region along the optical axis that, due to the paraxial approximation that provides the equations of section 2.3.1, is overestimated. This results in weaker radiation confinement in the focal region along the optical axis that can, at some extent, alter the dynamics of trapped nanostructures.

3.2 Numerical results for the radiation force

The first results we want to discuss concern the role played by the size of the spherical nano-structure in consideration of the accuracy of the optical forces simulations and performance in terms of computing time and CPU resources.

For FDTD simulation, on the basis of the strengths and weaknesses declared on technical notes, we decide to use the volumetric technique to determine the optical force as this approach is less sensitive to numerical noise, making it the better choice when the force is very small as in all our cases.

For T-matrix simulation, we run the jobs using a truncation of a series of multipole expansions to the order l=8 to ensure a suitable convergence.

In figures 12 and 13, we show the numerical comparison for the optical forces considering a single sphere with two different dimensions: in figure 12, we consider a radius of 5 nm; in figure 13 we consider a radius of 50 nm. In all cases, the spheres are illuminated by a TEM_{00} Gaussian beam propagating in the air along z-axes. The two panels regard the different numerical apertures of the focusing lens, addressing in this way two possible experimental situations, the first for optical tweezers with a lower spatial confinement of the electromagnetic field and the second with a higher spatial confinement. It is possible to note that, especially in the case of the 5 nm sphere, the agreement between the numerical data is excellent, even if the evaluation of the gradients of the linear part of the graph near the point of entrapment leads, for the three methods, to an estimate of the stiffness that can also differ substantially.

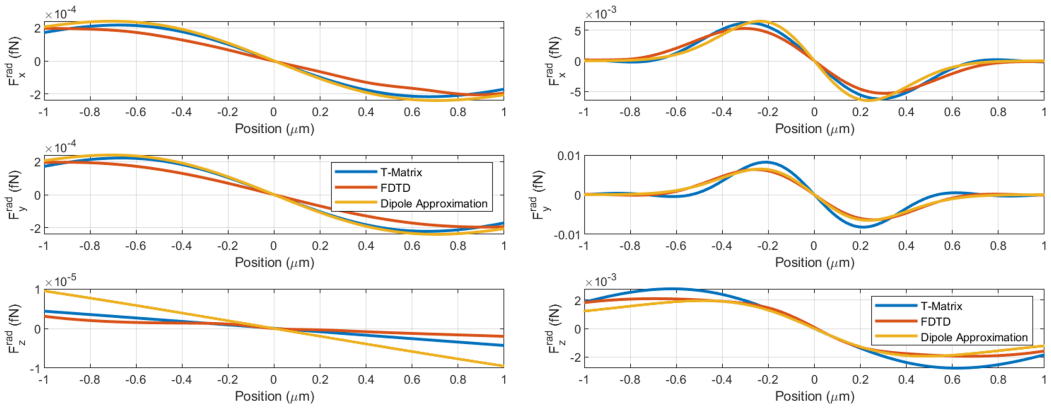

Figure 12: Optical forces on a nano-sphere along the coordinate axis due to a TEM_{00} Gaussian beam propagating in air along z-axes. The wavelength is λ=830 nm. The sphere has a radius of r_p=5nm and a refractive index of n_p=1.57. In the left panel, there is the numerical comparison for the results obtained in the T-matrix formalism, FDTD approach as implemented in Lumerical and Dipole Approximation, when the numerical aperture of the focusing lens is NA=0.3. On the right, the numerical comparison is for the optical forces for a numerical aperture of the focusing lens of NA=0.9.

In the case of the 50 nm sphere, we note that when the trap is made with a focusing lens of numerical aperture NA=0.3, the T-matrix and FDTD simulations show us that the sphere is not trapped, while a different result is obtained in the case the simulation is performed in dipole approximation. This discrepancy is mainly due to the fact that the simulations of the optical forces in dipole approximation provide reliable results as long as the condition x«1 is met: in this case, the size parameter is x=0.38.

In figures 14 and 16, we show the results regarding a 100 nm sphere in water in which we change the refractive index to consider the different behavior between a lower optical contrast scatterer, n_p=1.57, and a scatterer with higher optical contrast, n_p=2.4. Also, in this case, the FDTD simulations and those made with T-Matrix

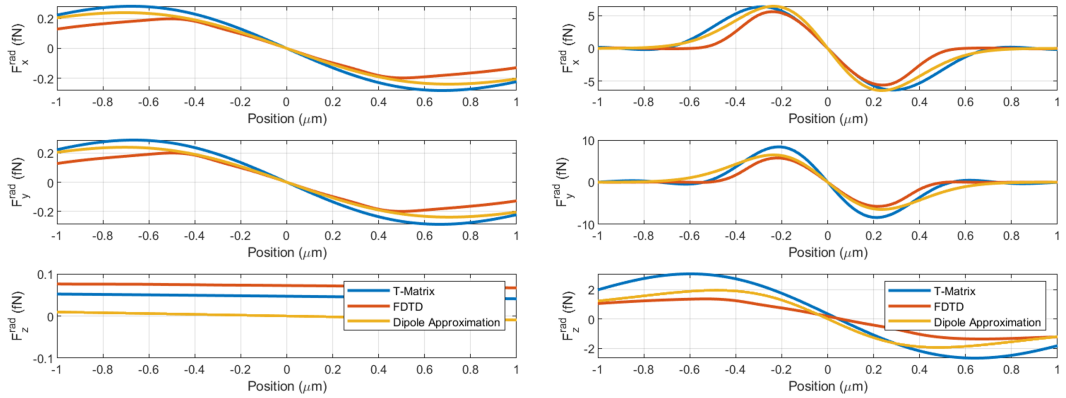

Figure 13: Optical forces on a nano-sphere along the coordinate axis due to a TEM_{00} Gaussian beam propagating in air along z-axes. The wavelength is λ=830 nm. The sphere has a radius of r_p=50nm and a refractive index of n_p=1.57. In the left panel, there is the numerical comparison for the results obtained in the T-matrix formalism, FDTD approach as implemented in Lumerical and Dipole Approximation, when the numerical aperture of the focusing lens is NA=0.3. On the right, the numerical comparison is for the optical forces for a numerical aperture of the focusing lens of NA=0.9.

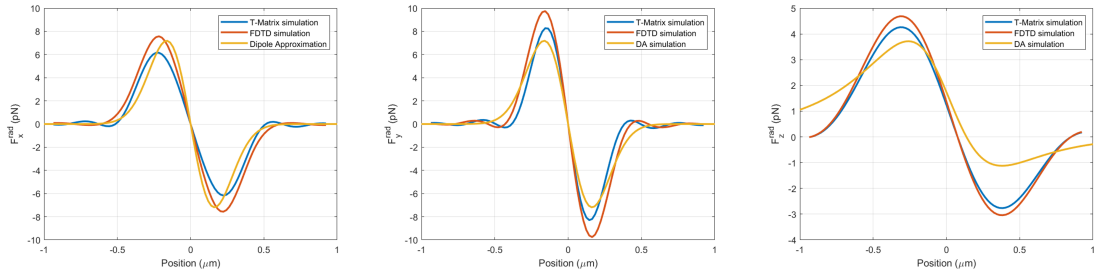

Figure 14: Optical forces on a nano-sphere along the coordinate axis due to a TEM_{00} Gaussian beam propagating in water along z-axes. The wavelength is λ=830 nm. The sphere has a radius of r_p=100nm and a refractive index of n_p=1.57. The numerical comparison of the results obtained in the T-matrix formalism, FDTD approach as implemented in Lumerical and Dipole Approximation, regards the case in which the numerical aperture of the focusing lens is NA=1.3.

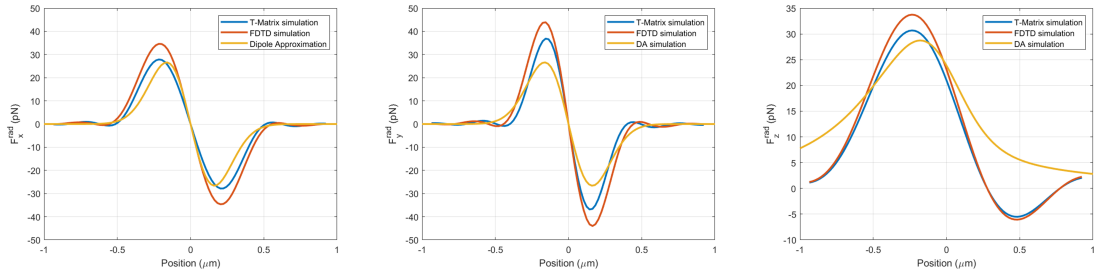

Figure 15: Optical forces on a nano-sphere along the coordinate axis due to a TEM_{00} Gaussian beam propagating in water along z-axes. The wavelength is λ=830 nm. The sphere has a radius of r_p=100nm and a refractive index of n_p=2.4. The numerical comparison of the results obtained in the T-matrix formalism, FDTD approach as implemented in Lumerical and Dipole Approximation, regards the case in which the numerical aperture of the focusing lens is NA=1.3.

have an excellent agreement, better than for the case for smaller scatterers, and the discrepancies obtained in dipole approximation are always due to the size parameter that now is about 0.8. The best agreement that is obtained in the case of larger nanostructures is essentially related to the choice of the coarse and fine mesh grid. If, in principle, the resulting discrepancies for smaller nanostructures can be eliminated by increasing the calculation points grid, this solution worsens the performance of the simulation not only in terms of time and memory resources but, above all, because the numerical rounding becomes relevant.

The last numerical comparison concerns the case of a dimer composed of two equal spheres with radius r=100 nm and refractive index n=2.4. The dimer in the upper panel of figure 17 is placed with the axis joining the centers along the x-axis, while in the bottom panel, the axis is directed along the axis of radiation propagation. Moreover, it was considered that the spheres that make up the dimer are not symmetrical with respect to the nominal focal point placed at x=0, y=0, and z=0.

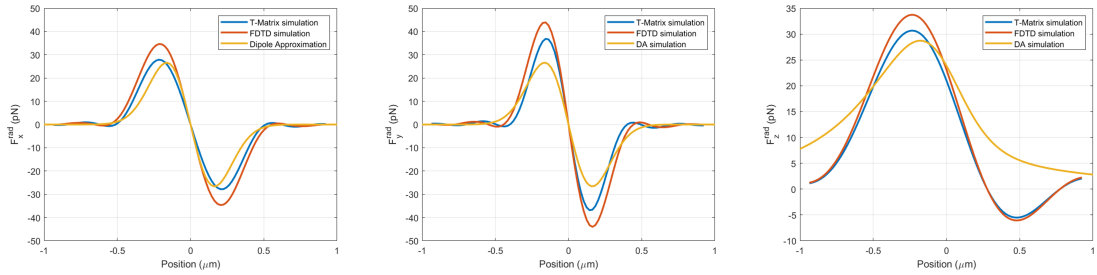

Figure 16: Optical forces on a nano-sphere along the coordinate axis due to a TEM_{00} Gaussian beam propagating in water along z-axes. The wavelength is λ=830 nm. The sphere has a radius of r_p=100nm and a refractive index of n_p=2.4. The numerical comparison of the results obtained in the T-matrix formalism, FDTD approach as implemented in Lumerical and Dipole Approximation, regards the case in which the numerical aperture of the focusing lens is NA=1.3.

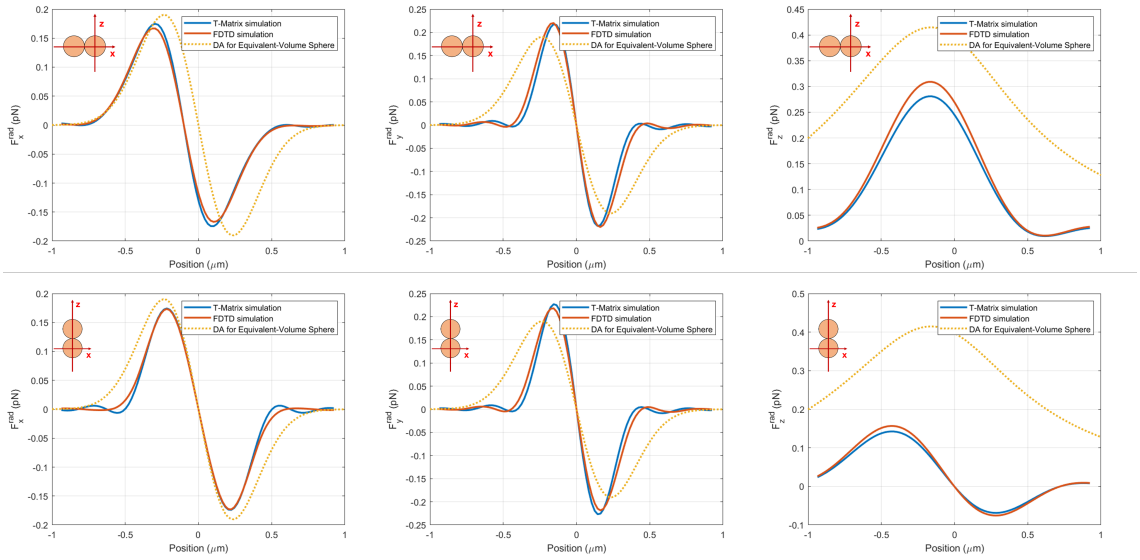

Figure 17: Optical forces on a 2-sphere cluster due to a TEM_{00} Gaussian beam propagating in water along z-axes. The wavelength is λ=830 nm. The spheres have a radius of r_p=100nm and a refractive index of n_p=1.57. The numerical comparison of the results obtained in the T-matrix formalism, FDTD approach as implemented in Lumerical, and the curves obtained in Dipole Approximation are for the equivalent-volume sphere with $r_p^{(e)}$=126 nm. The numerical aperture of the focusing lens is NA=1.3.

Moreover, it is considered that the spheres in the dimer are not symmetrical with respect to the nominal focal point at x=0, y=0, and z=0, as is evident from the analysis of the x-component of figure 17, upper panel. Again we compare the optical forces calculated according to the FDTD and the T-Matrix approaches. For comparison, in the figures, we also report the optical force calculated in dipole approximation for the equivalent-volume sphere with $r_p^{(e)}$=126 nm, showing that the optical forces of elongated nanostructures cannot be simulated using simple spherical symmetry models, since this latter, as is evident from the figures, do not correctly describe some specific characteristics.

It is necessary at this point to make some general considerations regarding the performance of the simulations in FDTD as implemented in the Lumerical software package. For this reason, in the following, we report some interesting data on the performance of the 100 nm sphere simulations.

To simulate the x-component of optical force in the chosen region that span the positions in the range (-1 μm +1 μm) we have required 30 equally distributed calculation points. To get fair results, we have defined a coarse meshgrid with a spacing of 25 nm and, around the nanosphere, a fine meshgrid with a spacing of 8 nm. For the 30 points needed for the simulation, the software allocated about 4.3 Gbyte of memory for the definition of the geometry and 2.8 Gbyte for the actual simulation of the optical force. To execute a job run, that is, to get the numerical result for the x-component of optical force, the software took a calculation time of about 4 hours on a workstation INTEL CORE i9. These performance values become

extremely critical in the case of the 5 nm sphere simulation. In this case, the adopted fine meshgrid has a spacing of 0.8 nm, and the execution time was of more than 60 hours.

3.3 Numerical comparison: comments and conclusions

The transition matrix (T-Matrix) method and the finite-difference time-domain (FDTD) method are widely used numerical techniques for studying the interaction of electromagnetic waves with particles, including calculating optical forces. Here are some key differences between the two approaches:

1. *Geometrical constraints*: The FDTD method is typically better suited for handling non-spherical or non-symmetric particle geometries as far as the geometrically complex nano-structure cannot be simulated as an aggregate, whereas the T-Matrix approach, as implemented by a code that makes use of vector multipole field expansion, is more suitable for spherical particles in a wide range of size parameters and when the geometry can be simulated as an aggregate of different spheres, possibly also radially non-homogeneous.

2. *Speed*: In the studied cases, the FDTD method, as far as requires less computational resources, proves to be slower than the T-Matrix method. This is because the FDTD method is based on solving iteratively the Maxwell's equations on a numerical grid, while our implementation of T-Matrix approaches is fast as it involves the analytic complex numerical integration necessary to calculate the forces, which results in the computation of incident and scattered coefficients.

3. *Accuracy*: The T-Matrix method can be considered more accurate than the FDTD method for calculating optical forces, particularly for spherical nanostructure and/or their aggregate. This is because the T-Matrix method carefully describes the electromagnetic interaction, also including multiple scattering effects.
4. *Physical insights*: The T-Matrix method provides physical insights into the scattering process, including information on the angular distribution of scattered light and the polarization of the scattered light. The FDTD method is a black-box approach and provides less physical insight.
5. *Flexibility*: The FDTD and T-Matrix methods are very flexible in terms of their ability to handle a wide range of material properties, such as anisotropic materials and dispersive materials. However, the T-Matrix method is generally limited to handling linear materials or systems that possess sharp edges.

In summary, the T-Matrix and the FDTD methods have their advantages and limitations, and the choice of which method to use depends on the specific application and the geometrical and material properties of the particle under study.

Here are some other differences between the T-Matrix method and the FDTD method for calculating optical forces:

- Near-field vs. far-field interactions: The T-Matrix method is generally more suitable for calculating near-field interactions between particles and electromagnetic waves, whereas the FDTD method is more helpful in studying far-field interactions. This is due to the fact that the T-Matrix approach is based on the solution for the particle's scattering coefficients, which provides

information on the electromagnetic field in the near-field region around the particle. The FDTD method, on the other hand, is typically used to simulate the propagation of electromagnetic waves in the far-field region, as when calculating scattering or diffraction patterns.

- Boundary conditions: The FDTD method, in contrast to what is necessary for the T-Matrix approach, requires specifying the boundary conditions at the edges of the computational domain, which can be challenging for complex geometries or non-uniform materials.

- Multiple scattering effects: The T-Matrix method can be extended to handle various scattering events, which can be important for understanding the interaction of light with densely packed or clustered particles. The FDTD method, on the other hand, typically assumes that the particles are well-separated and does not explicitly account for multiple scattering effects.

Overall, the choice between the T-Matrix method and the FDTD method for calculating optical forces, regardless of the simulation performance, will depend on the specific situation, including the geometrical and material properties of the particles, the desired level of accuracy, and the computational resources available.

In the next chapters, due to the complexities of simulations that involve large and non-homogeneous spherical scatterers, spherical monomers with inclusions, aggregates with different morphology, and poly-dispersion of metal nano-particles, we use almost exclusively the simulation codes based on T-Matrix approach.

Chapter 4

Modeling optical forces for space tweezers applications

The investigation of dust grains in space is an important area of research, as these particles play a dominant role in the formation and evolution of planetary systems. However, studying dust grains in space poses several challenges, such as their small size and irregular shape, which makes it difficult to manipulate and observe them. In recent years, optical tweezers have emerged as a promising tool for studying small particles in various contexts, including biology and materials science. Cosmic dust refers to small, solid particles typically ranging from a few nanometers to several tenths of millimeters. These particles are found dispersed throughout the interstellar medium and interplanetary space within the solar system. The formation of interstellar dust particles is a multifaceted phenomenon that arises from a complex interplay of diverse astrophysical processes associated with the life cycles of successive generations of stars. These intricate mechanisms include the ejection of dust particles through various channels, such as radiation pressure, solar wind, and explosive events that occur during the final stages of stellar evolution or the shedding of outer layers [52, 53, 54]. These processes release different dust particles with various physical and chemical properties that play a crucial role in shaping the evolution of galaxies and the interstellar medium. The investigation of cosmic

dust has emerged as a vital area of interest within the astrophysical sciences. It is fueled by its pivotal role in different cycling processes that operate throughout the universe. In this context, interplanetary dust has gained significant attention as a rich source of scientific inquiry. Composed of small, solid particles that arise through various mechanisms, including collisions between celestial bodies and the sublimation of icy bodies [55], this dust plays a critical role in shaping the dynamics of the interplanetary environment and influencing the evolution of planetary systems. As such, its study has become an essential focus of many research efforts to enhance our understanding of the complex astrophysical processes that govern the universe. Interplanetary dust is a valuable source of information for astrophysical research, as it provides an opportunity for direct analysis of these elusive particles through various sample-return missions. These missions offer a unique tool for studying the physical and chemical properties of interplanetary dust in detail, which is impossible through remote observations alone. The samples are collected from various sources within the solar system, including the interplanetary medium, planets, and minor bodies [56, 57, 58], as well as from the Earth's stratosphere [59, 60] and surface in the form of micrometeorites [61]. To gain insights into the properties of these particles, the samples are subjected to advanced analytical techniques at terrestrial facilities, as some of the necessary instruments are too large to be deployed in space [62]. The resulting data has contributed significantly to our understanding of the origins and distribution of interplanetary dust, enabling us to develop a more comprehensive picture of the complex astrophysical processes that shape our solar system. The current chapter explores the precise calculation of optical forces in the

T-matrix formalism, particularly emphasizing the pivotal influence of composition and complex morphology in the optical trapping of cosmic dust particles. By shedding light on these fundamental aspects of optical manipulation, we aim to advance our understanding of the underlying physics and open up new possibilities for the application of optical tweezers in a range of extraterrestrial environments. Specifically, our findings hold important implications for using optical tweezers in curation facilities for sample return missions, where accurate optical trapping can enable the manipulation and analysis of tiny, delicate particles that may hold crucial clues to the origins and evolution of our solar system.

4.1 Space Tweezers

Optical Tweezer is a potential application for studying dust grains in space, such as characterizing the physical properties of grains and their interactions with other particles. Despite the impressive advances in optical trapping techniques and their application in many research fields, their use in planetary exploration has yet to be fully realized, although it has been considered by organizations such as NASA [63]. Optical trapping technology for the collection and in-situ analysis or return to Earth of a wide range of extraterrestrial particles would provide unprecedented insights into space materials currently beyond our reach. For example, volatile dust components that cannot be detected in situ by instruments such as GIADA, MIDAS, and COSIMA on the Rosetta/ESA mission or that are subject to biases due to sample collection media contamination, such as the cometary dust samples

retrieved by the Stardust/NASA space probe [64, 65] and trapped in aerogel. Therefore, the development and implementation of optical trapping techniques for planetary exploration would offer a unique opportunity to expand our understanding of the composition and properties of extraterrestrial materials, unlocking new avenues of scientific exploration in the field of planetary science. Within the field of space exploration, the Space Tweezers project (https://www.spacetweezers.org) has emerged to develop optical tweezers (OT) methodologies for trapping and spectroscopically characterizing extraterrestrial dust particles and their analogs using Raman tweezers. The results of this study will establish a firm foundation for the future use of OT techniques in the exploration of the solar system, including the analysis of cometary particles, the volatile components of such particles, and the dust particles found in the Martian atmosphere and on the Martian and Lunar surfaces. Additionally, the use of OT in preliminary sample characterization in curatorial facilities for samples returned from space missions will be strategically valuable.

4.2 The Complexity of Solar System Dust

A significant amount of dust particles characterizes the interplanetary space in the solar system. This phenomenon is evident to the unaided eye through the Zodiacal Light, a faint cone of light visible above the eastern horizon before sunrise or above the western horizon after sunset. Similar to how the Milky Way showcases the multitude of stars comprising our galaxy, the Zodiacal Light [11] displays a vast quantity of fine dust particles that scatter solar radiation throughout the

interplanetary space of the solar system. The interplanetary dust complex consists of microscopic (mainly rocky) particles, typically less than a few millimeters in size, called micrometeoroids, moving in the interplanetary space of the solar system [66]. Dust is produced by collisions among solid bodies [67, 68], by disruptions of icy bodies, and by cometary activity [69, 70]. As such, the interplanetary dust complex derives from Cosmo chemical analyses of samples recovered from Earth's 1) surface, e.g., micrometeorites collected in Antarctica [71, 72]; 2) stratosphere, by balloon born instruments as eg., DUSTER, designed for a non-destructive and uncontaminated collection of solid particles from tens of microns down to 200 nm in size [73] and by stratospheric NASA/ aircraft passive sticking on silicon oil coated plates [74]. A critical contribution is also given by laboratory analyses of samples [64, 65]. In addition, cometary dust was studied in situ from the onset of cometary activity to its cessation after perihelion by the Rosetta/ESA space mission [75, 76].

4.3 Optical forces on dust particles

4.3.1 Models for dust particles

In an astrophysical environment, the variety of dust particles necessitates the development of sophisticated models to calculate the optical forces required for space tweezers applications. We consider several models of extraterrestrial dust with shape and composition inspired by interstellar particles, DUSTER samples [81], and Moon or Mars dust analogs. Some examples are shown in figure 18. However, it is clear

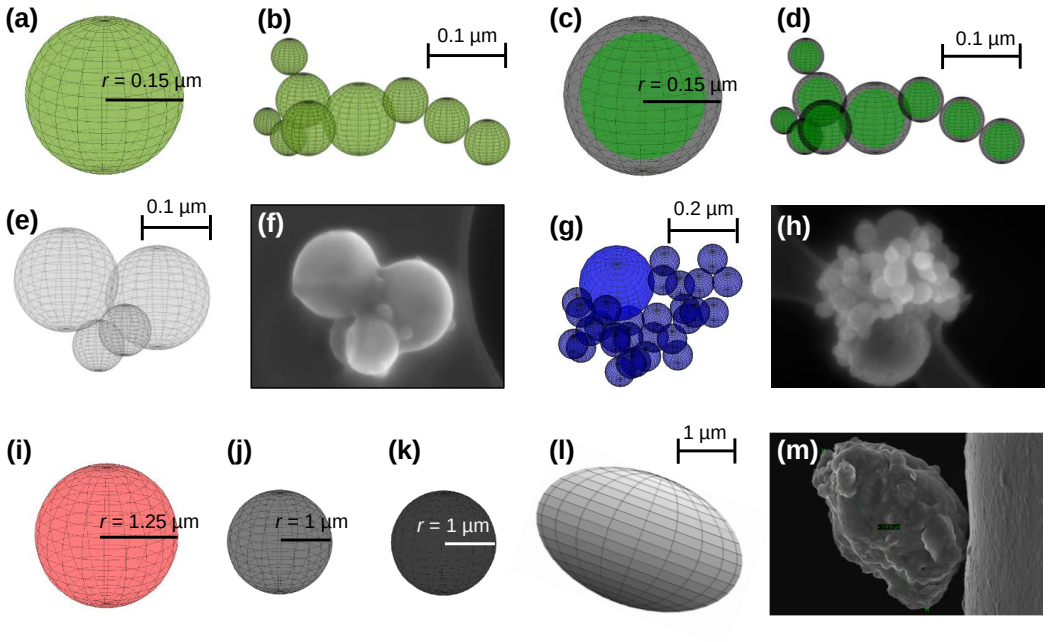

Figure 18: Scattering models with shape and composition inspired by interstellar, interplanetary (DUSTER mission [77]), and planetary [78] particles. On the top, the models emulate hypothetical interstellar dust grains whose constituents are olivine and aliphatic carbon. In (a) and (b), the constituent's refractive indexes are mixed according to the Bruggeman criterion. Instead, in (c) and (d), the olivine is considered covered by a carbon layer. In (e), the model of a silica particle arranged in quenched melt spheres is shown in the FESEM image [77] (f). In (g), the model of condensed Ca[O] nanograins that are accreted onto a larger melted aggregate of tiny carbonate grains shown in the FESEM image [77] (h). The larger sphere is calcite, and the other spheres are CaO. In (i), a spherical model of the particle Fe, Mg-rich 'TP2' [79], in which an effective refractive index is considered by mixing iron (67%) and magnesium (33%). In (j), a spherical model of Martian hematite [78]. In (k), a spherical model of Lunar regolith [80]. In (l), a model of an ellipsoidal fassaite is shown in the FESEM image (m). Here, an effective refractive index is considered by mixing silica (53%), CaO (27%), FeO (10%), Al_2O_3 (10%). (from Ref. [11]).

that the diversity of dust particles in an astrophysical context implies a richness of models that need to be developed to calculate optical forces posing a computational challenge. While for model spherical particles, such forces can be calculated by using exact electromagnetic solutions of the scattering problem, realistic dust grains are far from exhibiting these simple shapes, as shown in Fig. 18. Aiming to replicate realistic dust scattering properties, different model particles have been proposed that include aggregates, stratified, agglomerate debris, or Gaussian random particles. While the use of these more sophisticated model geometries represents better the physical reality, the increased detail in the morphology comes with the drawback of a higher demand for computational power, limiting the number of configurations that can be numerically explored.

4.3.2 Modelling optical trapping of dust particles in laboratory optical tweezers

From the experimental point of view, optical tweezers have been mostly employed to trap and manipulate micron-sized objects in a liquid environment rather than in air or in a vacuum. This is because liquid media minimize the effects of external perturbations on a trapped particle and the effect of inertia on its dynamics, while trapping in air or vacuum is more challenging. In fact, the trapping stability can be affected by external perturbations generated by airflows, acoustic shocks, thermal drift, mechanical vibrations, and even by the intensity noise of the trapping laser. Furthermore, liquid media can suspend the particles for a long time before and

after trapping, allowing the selection and trapping of a specific single particle over a multitude. For these reasons, in Ref. [6], some novel experiments on optical trapping and spectroscopic characterization of cosmic dust particles and analogs have been achieved in a liquid environment. We performed accurate optical trapping calculations in the T-matrix formalism, highlighting the key role of composition and complex morphology in the optical trapping of these cosmic dust particles.

The samples trapped in the CNR-IPCF laboratory [6] have known textures and mineralogic compositions. The aim is to use this information to model the optical trapping properties of cosmic dust particles and analogs.

The samples considered have terrestrial and extraterrestrial origins. They are (1) a hawaiite from Etna volcano in Italy (HE-1), (2) the CV3-OxA carbonaceous chondrite Allende (A-1), and (3) a lunar poly-mixture regolith breccia meteorite found in Antarctica (DEW 12007) [82]. The mineralogy composition of these samples is shown in figure 19.

For the experimental investigation of the optical trapping properties of single grain dust particles, a home-built optical tweezers were used. An optical trap is generated by highly focusing a laser beam through an objective, the trajectory of the trapped particle is then acquired by a quadrant photodiode and analyzed by a computer to characterize optical forces and rotations arising from the interaction of the particle with light. From these measurements, the stiffnesses of the effective optical trapping potential are obtained experimentally. These quantities can then be compared with our T-matrix calculations.

XRD results	Main mineralogy	%
HE-1 – Hawaiite	Plagioclase: labradorite	56
	Clinopyroxene: augite	35
	Olivine: forsterite	8
	Magnetite	0.01
	Glass	0.99
Allende – CV3 OxA	Olivine: forsterite	80
	Clinopyroxene: clinoenstatite	9
	Clinopyroxene: diopside	7
	Orthopyroxene: enstatite	2
	Clinopyroxene: pigeonite	1
	Chromite	0.99
DEW 12007 – Lunar regolith breccia	Plagioclase: labradorite	48
	Clinopyroxene: augite	23
	Clinopyroxene: pigeonite	18
	Olivine: forsterite	10
	Ilmenite	1
	Chromite	0.001

Figure 19: XRD results for the mineralogy of the samples HE-HA Hawaiite, Allende-CV OxA, DEW 12007-Lunar regolith breccia and the compositions of the samples with their percentages (Done in CISUP, Pisa University).

To accurately calculate the optical trapping of dust particles using the T-matrix formalism, following the dimensions given by the SEM images (Fig. 20), we first modeled the particles as microspheres with a diameter close to their average size of 1 μm, despite their irregular shape. The incident radiation was modeled to reproduce the characteristics of the laser beam used in the experiments as a Gaussian laser beam with a wavelength $\lambda = 830$ nm and a power P=50 mW, focused by a NA objective for air NA=0.9, for water NA=1.3. We modeled the particles taking proper account of their mineral composition, and adopted two strategies. In the first case, we used a single sphere model, see figure 21 panel (a), with an effective refractive index obtained

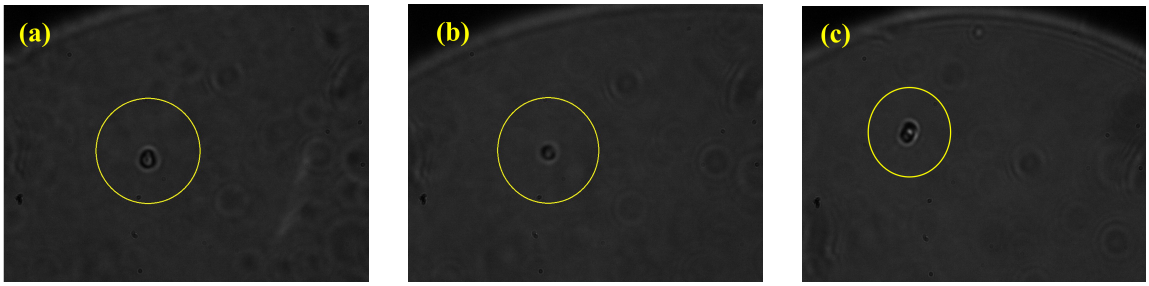

Figure 20: Optical microscope images (a) HE-HA Hawaiite Diameter 2.91 μm (b) Allende-CV OxA Diameter 1.32 μm (c) DEW 12007-Lunar regolith breccia Diameter 1.05 μm (Done in CNR Messina)

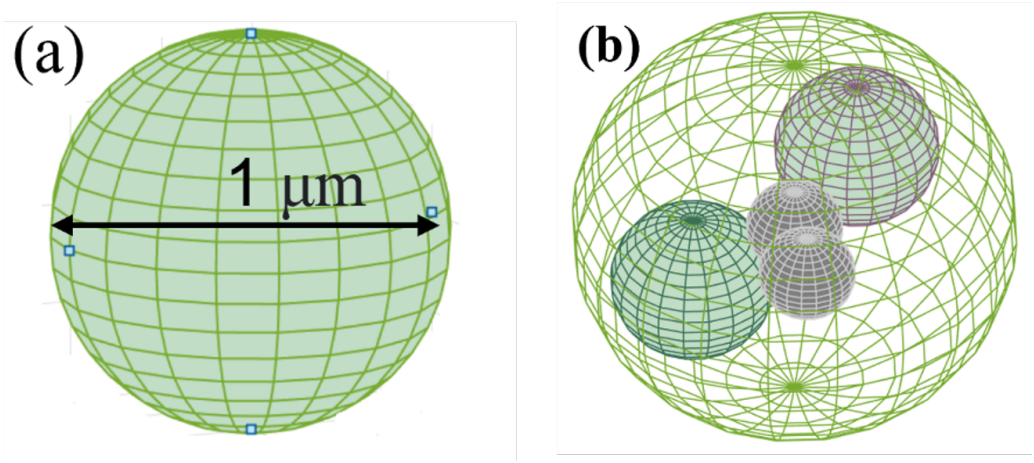

Figure 21: (a) Single sphere with an effective refractive index obtained according to the Bruggeman Mixing Rule (b) Non-homogeneous distribution where the external sphere is made by the dominant material in the mixture, while the inclusions are made of materials representative of the variety of materials resulting from XRD analysis.

according to the Bruggeman Mixing rule [83]. In the second model, we used a sphere composed of the material mostly present in the mixture, containing some inclusions, see figure 21 panel (b). The size and the composition of these inclusions are chosen in such a way that they can better represent the variety of materials resulting from XRD analysis, see table 19 for reference.

The values used for the mixing were summarized in Table 22. The refractive index of olivine was provided by Draine and Li, while that of carbon was provided by Ashok et al. [84, 85]. The inclusions are made of the secondary constituents, as listed below:

- **HE-1-Hawaite:** Two inclusions made of olivine, each having a volume fraction of 8%, and two inclusions of magnetite, each having a volume fraction of 1%.
- **Allende CV3 OxA:** Two inclusions made of clinoenstatite and enstatite, each having a volume fraction of 12%, and two inclusions of diopside and pigeonite , each having a volume fraction of 8% (see Table 19).
- **DEW 12007-Lunar Meteorite:** Two inclusions made of olivine, each having a volume fraction of 10%, and two inclusions of ilmenite, each having a volume fraction of 2%.

HE-1-Hawaite										
	Plagioclase		augite		Olivine		Magnetite			
	n	k	n	k	n	k	n	k		
	1.56	0	1.573	3.10E-05	1.63	3.0E10-4	2.253	0.143		
Ɛ1	2.4336		2.47433E+00		2.657		5.05556			
Ɛ2	0		9.75260E-05		9.7E10-4		0.644358			
Ɛ1tot	2.464									
Ɛ1tot	4.65E-04									
Allende CV3 OxA										
	Olivine: forsterite		clinoenstatite		diopside		enstatite		pigeonite	
	n	k	n	k	n	k	n	k	n	k
	1.63	3.00E-04	1.573	3.10E-05	1.623	2.80E-03	1.618	1.351E10-4	1.573	0.000423
Ɛ1	2.657		2.47300E+00		2.63412116		2.657		2.474328821	
Ɛ2	9.7E10-4		1.33E10-3		0.0090888		4.37E10-4		0.001330758	
Ɛ1tot	2.634									
Ɛ2tot	0.155E10-2									
DEW 12007-Lunar Meteorite										
	Plagioclase		augite		pigeonite		Olivine		Ilmenite	
	n	k	n	k	n	k	n	k	n	k
	1.56	0	1.573	3.10E-05	1.573	4.23E-04	1.63	3.00E-04	2.4	0.3
Ɛ1	2.4336		2.47433E+00		2.47433E+00		2.657		5.67	
Ɛ2	0		9.75260E-05		1.33076E-03		9.7E10-4		1.44	
Ɛ1tot	2.493									
Ɛ2tot	0.734E10-2									

Figure 22: Refractive index and dielectric constants calculated using the Bruggman mixing Rule for HE-1-Hawaite, Allende CV3 OxA, and DEW 12007-Lunar Meteorite. The refractive indices used were provided from [84, 85, 86, 87, 88, 89]

4.3.3 Results

We conducted a study to analyze the trapping stiffnesses of three samples: HE-1-Hawaite, Allende CV3 OxA, and DEW 12007-Lunar Meteorite, when these scatterers are immersed in water and air, see figure 23. Here, we consider for the simulation nanospheres with d=1μm and used for dielectric constants the data reported in table 22. These dielectric constants were calculated through the Bruggman mixing rule, starting from the dielectric constants of the single material components. By analyzing figure 23 (b), (d) and (f), these kind of nanoparticles are all trapped when they are immersed in water, as Q_z goes to 0 with a negative gradient. In the case that the external medium is air, even if the efficiencies Q_x, Q_y are able to confine the scatterers, the radiation force, Q_z, pushes out the particles as it never reaches 0.

In Figure 24, we present the transverse, x, y, and longitudinal, z, stiffnesses as a function of the particle radius when the scatterers are immersed in water. Additionally, we found that the stiffnesses decreased almost linearly with the radius for all considered cases. The difference between the stiffnesses along the x and y directions can be attributed to the polarization of the incident field, as we used a Gaussian beam TEM_{00} x-polarized field. Typically, the stiffnesses values along the z direction were lower than those along the x and y directions, as the radiation pressure tends to destabilize the particle along the z-axis. For the model presented in figure 21 (b), which takes into account the real dis-homogeneity of the simulated grain, we were able to compare the theoretical results with the experimental ones. For this reason, we report the results obtained in the next section.

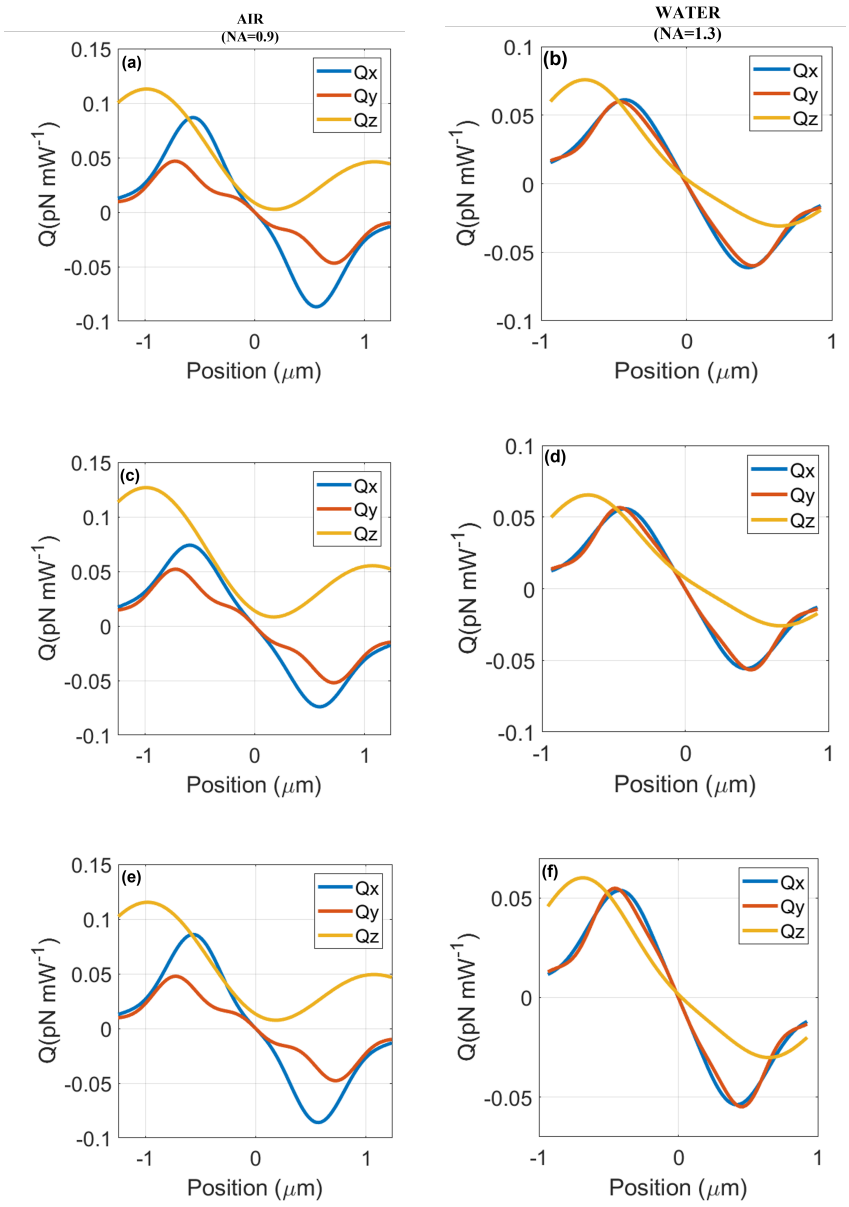

Figure 23: The trapping efficiencies (Q_x, Q_y, Q_z) of these three samples (a) and (b) HE-1-Hawaite, (c) and (d) Allende CV3 OxA, and (e) and (f) DEW 12007-Lunar Meteorite respectively in air (n_m=1) and in water (n_m=1.33) in the transverse, x, y, and longitudinal, z, directions, as a function of displacement from the nominal paraxial focus.

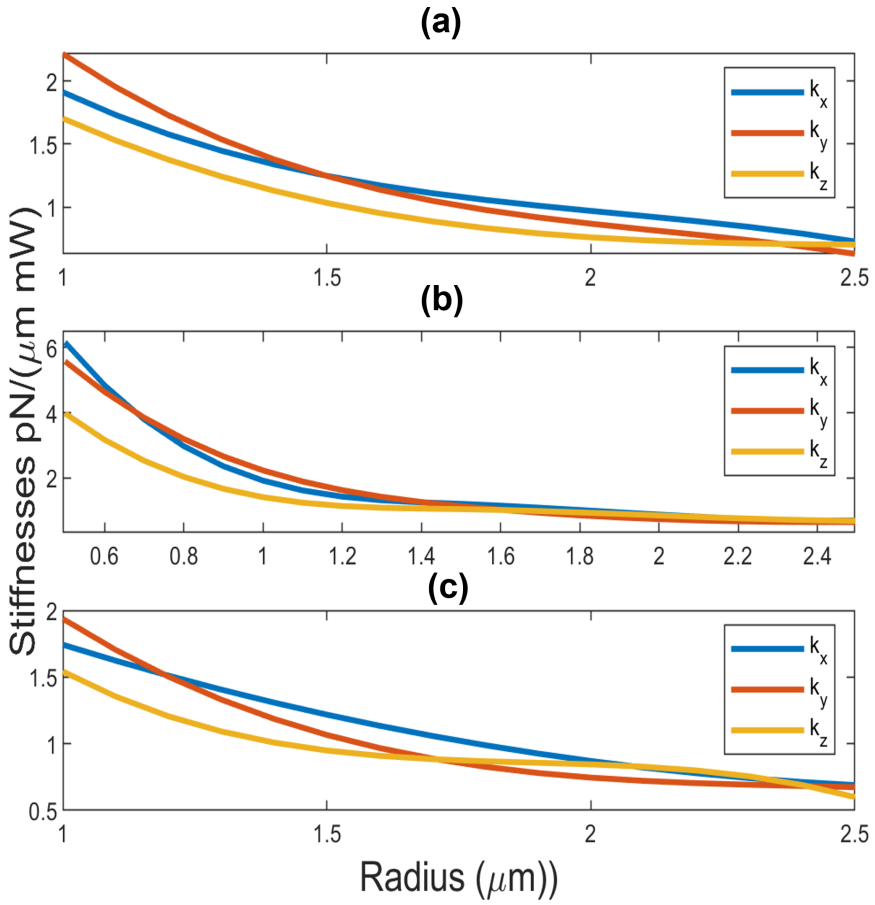

Figure 24: Trapping stiffness k_x, k_y, k_z as a function of the particle radius in the transverse, x, y, and longitudinal, z, directions, for the three samples (a) HE-1-Hawaite, (b) Allende CV3 OxA, and (c) DEW 12007-Lunar Meteorite immersed in water.

4.3.4 Comparison with experiments

In order to compare the experimental results with our theoretical simulations, we consider particle models emulating the dust grains of the lunar meteorite DEW 12007. Although all the trapped dust grains showed irregular shapes, for simplicity, we modelled our particles as micro-spheres having an average diameter $d = 1$ μm with a refractive index given by the Bruggeman mixing rule for the constituent minerals of DEW 12007 (as shown in Fig. 21 and Fig. 25).

Here we consider a laser beam tightly focused by a high-NA objective (NA=1.3), mimicking the experimental conditions used during the investigation of the lunar dust grains in Ref. [6]. In figure 25(a), we show the theoretical transversal and longitudinal trap efficiencies defined respectively as $Q_{xy}^{\mathrm{th}} = (F_x^{\mathrm{opt}} + F_y^{\mathrm{opt}})/2\mathrm{Pw}$ and $Q_z^{\mathrm{th}} = F_z^{\mathrm{opt}}/\mathrm{Pw}$. Thereafter, we refined our particle model to take into account the anisotropy and heterogeneity of the real dust grains. We still considered a homogeneous sphere, with a refractive index obtained according to the Bruggeman mixing rule, but now we add 4 spherical inclusions, 25(b) inset. These inclusions are made of the secondary constituents of the lunar meteorite, in particular, we consider 2 inclusions made of olivine having a 10% each of the total volume of the modelled grain, and 2 inclusions of ilmenite with a 2% each of the total volume. Similarly to the previous model, we calculate the optical forces and the theoretical longitudinal trap efficiency Q_z^{th}, as shown in Fig. 25(b). Here it is possible to notice how the trap efficiency is affected by the internal structure of a dust grain, presenting several equilibrium points with $Q_z^{\mathrm{th}} = 0$, and only two stable equilibrium points at $x = -0.38$ and $x = 0.75$ μm,

conversely, the homogeneous model was showing an only stable equilibrium point at $x = 0$ μm, Fig. 25(a,b).

After computing the theoretical optical forces acting on our model particles and their stiffnesses, we compare the theoretical and experimental mean transverse stiffness efficiencies $q_{xy} = (q_x + q_y)/2$ and longitudinal stiffness q_z, Fig.25(c), to validate our theoretical model. In figure 25c, it is possible to notice a fairly good agreement between the theoretical and experimental values of the stiffness efficiencies q^{th} and q^{ex}, validating the theoretical model used for the calculation of optical forces acting on cosmic dust. The small discrepancies are due to the spherical shape used in our model which is a simplification of the complex particle shape, mass distribution, and mineral composition.

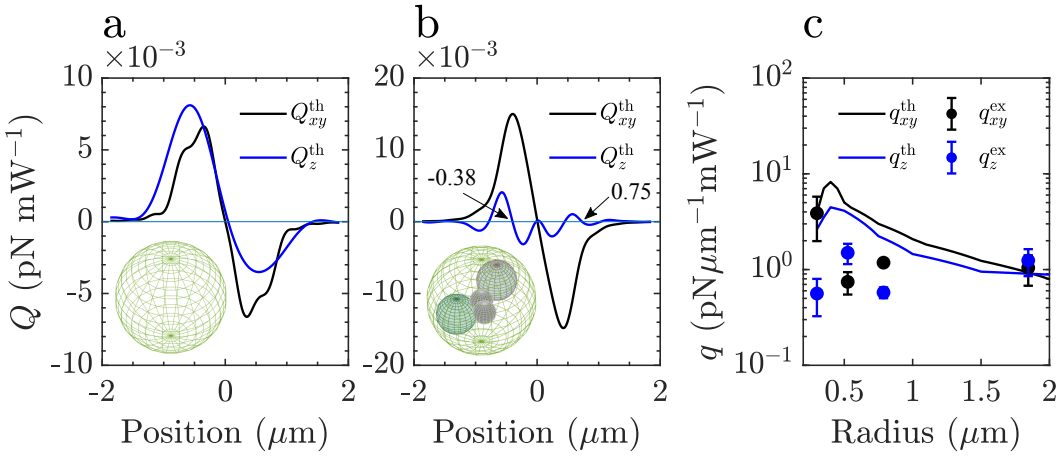

Figure 25: Comparison with experimental results of Ref. [6]. a) Dark blue line represents the theoretical trap efficiency $Q_z^{\rm th}$ along the longitudinal direction z with $x = y = 0$. Black line represents the theoretical trap efficiency $Q_{xy}^{\rm th}$ along the transversal direction $x - y$ with $z = 0$. In the inset is shown the theoretical particle, modelled as a micro-sphere with a homogeneous refractive index according to the Bruggeman mixing rule. Light blue line is a reference line at $y = 0$. b) Dark blue line and black line represent the theoretical trap efficiency $Q_z^{\rm th}$ and $Q_{xy}^{\rm th}$, respectively, for the particle model showed in the inset. Here the particle is modelled as a micro-sphere with a homogeneous refractive index according to the Bruggeman mixing rule and has 4 inclusions made of the secondary constituents of the lunar meteorite, 2 inclusions made of Olivine having a 10% each of the total volume and 2 inclusions of Ilmenite with a 2% each of the volume. $Q_z^{\rm th}$ presents only two stable equilibrium points at $x = -0.38$ and $x = 0.75$ μm, but, according to our forces calculations, only at $x = 0.75$ μm trapping along the x and y direction is possible. c) Theoretical (lines) and experimental (dots) stiffness efficiencies q_{xy} and q_z within the transversal plane $x - y$ and along the longitudinal direction z, respectively. Blue lines and dots represent the theoretical and experimental efficiency $q_{xy}^{\rm th}$ and $q_{xy}^{\rm ex}$ respectively, along the transversal direction $x - y$, while the black lines and dots represent the theoretical and experimental efficiency $q_z^{\rm th}$ and $q_z^{\rm ex}$ respectively, along the longitudinal direction z.

Chapter 5

On the optical properties of Ag-Au colloidal alloys

In this chapter we present simulations regarding the optical response in the UV-Vis range of colloidal Ag-Au solutions, obtained through a laser ablation process with controlled parameters, applying the T-matrix approach [13] [12]. Through these simulations, as long as the particles formed in the experiment can be considered spherical monomers (possibly aggregated), it is possible to understand with no ambiguity whether from the peculiar shape of the UV-Vis spectra of nano- composites can be extracted information related to the effective formation of a metal alloy. In addition, our theoretical approach, once fed by the appropriate optical constants, allows a reliable design of the surface plasmon resonance (SPR) of the nanoparticles (NPs) that constitute the colloids according to the main process parameters, namely the composition of the Ag-Au mechanical mixture leading to the alloy, and the NP average size.

The samples we theoretically studied are:
(a) elemental colloidal suspensions of Ag and Au NPs (from now on referred to as e-Ag and e-Au) prepared using PLAL in distilled water, using a pulsed laser at 532 nm wavelength. In figures 26 (a) and (b) we show the SEM picture we used to characterize the size and the morphology for the as-prepared colloidal dispersion
(b) physical mixtures constituted taking selected volume fractions from the elemental

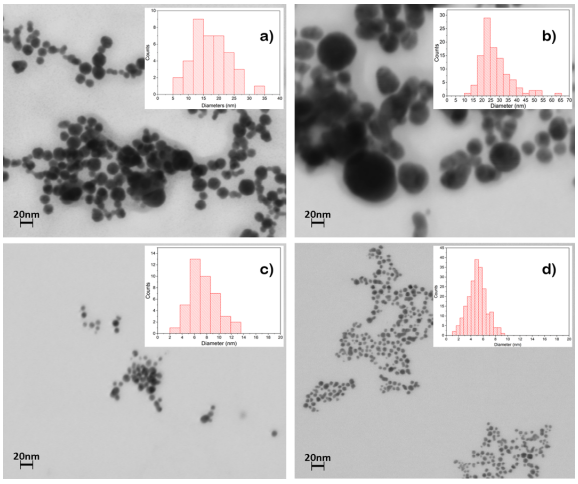

Figure 26: Elemental NPs prepared by PLAL at f = 10 Hz, t = 20 min, F = 1.5 J cm^{-2}: a), e-Ag; b), e-Au. Elemental NPs re-irradiated at f = 10 Hz, t = 120 min, F = 1.2 J cm^{-2}: c), r-Ag; d), r-Au. (f is the laser repetition rate, F is the laser fluence and t is the exposure time)

colloids and mixing them.

(c) re-irradiated of both elemental colloids (from now on referred to as r-Ag and r-Au), see figures 26 (c) and (d), and physical mixtures through the laser source used for the synthesis, at the same wavelength, for 120 minutes at the laser fluence of 1.2 J cm^{-2}. In figure 27, we show the representative morphology and size histogram of m-Ag50Au50 (physical mixture, panel a) and the typical morphology of r-Ag50Au50 (re-irradiated NP mixture, panels b, and c)

We recall here that through the definition of the normalized scattering amplitude, see equation 1.3.3, it is possible to define the extinction cross section (equation 1.3.3) that is the key quantity that enters in the simulations for the UV-Vis spectra obtained for the samples briefly described above. For clarity, in the following, we will discuss the obtained results by discussing individually all the different studied cases.

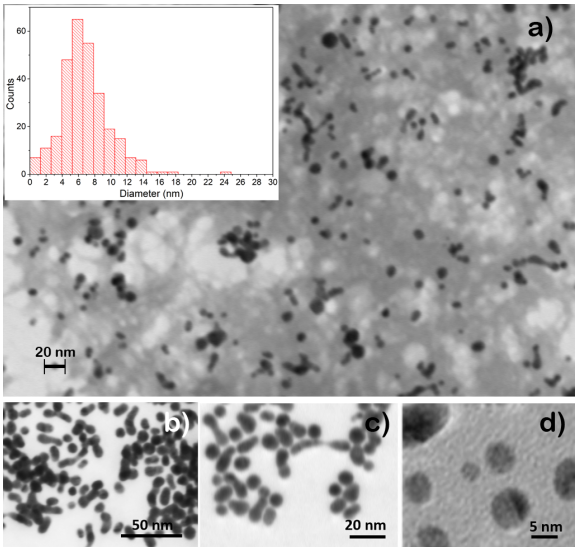

Figure 27: Representative morphology and size histogram of m-$Ag_{50}Au_{50}$ (physical mixture, panel a); typical morphology of r-$Ag_{50}Au_{50}$ (re-irradiated NP mixture, panels b and c); TEM high magnification pictures of selected NPs (panel d).

5.1 Simulations of the UV-Vis spectra for pure metal colloids (e-Ag and e-Au)

In Figure 28, we collect the optical properties of the elemental NPs as represented by the extinction spectra, both measured (red lines, experiment) and calculated (blue lines, theory). For as-prepared Ag NPs (e-Ag), a single peak centered at 407 nm with FWHM of 70 nm is a marker of isolated, spherical particles (Figure 28a). Figure 28c shows the extinction spectrum of as-prepared Au NPs (e-Au), a single feature peaked at 526 nm, with FWHM of about 80 nm. After the laser re-irradiation (120 min) for both metals, we observe a slight blue shift of SPR (for Ag, from 407 down to 400nm; for Au, from 526 to 522 nm). Particularly, the FWHM decreases to 55 nm for Ag and remains almost unchanged for Au (Figure 28d). In agreement with

recent observations [90, 91, 92] we conclude that re-irradiation with ns laser pulses produces a consistent particle fragmentation in the colloids of both metals.

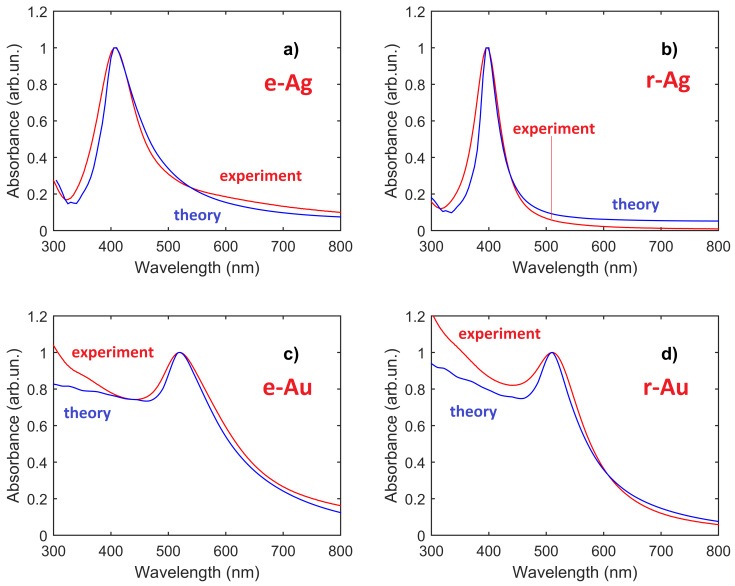

Figure 28: Extinction spectra of elemental NPs: Ag (as prepared, e-Ag panel a; re-irradiated, r-Ag panel b) and Au (as prepared, e-Au panel c; re-irradiated, r-Au panel d). In all panels red curves, labeled experiment, refer to experimental data; blue curves, labeled theory, refer to best fits from theory – see Methods.

Now, as regards the theoretical UV-Vis spectra obtained for the two elemental samples, we consider that the e-Ag and e-Au colloids are polydispersed in size and, in the limit of low dilution, we determine the optical properties of both elemental colloids through a weighted average of particles sizes, from $r_{min} = 1$ nm to $r_{max} = 300$ nm, of single particle extinction cross-sections calculated as briefly reported in the preceding section

$$\langle \sigma_{ext} \rangle = \int_{r_{min}}^{r_{max}} dr\, n(r)\, \sigma_{ext}(r) \tag{33}$$

	r_{av} (nm)	σ	r_{min} (nm)	r_{max} (nm)
e-Ag	30	1.5	1	300
r-Ag	25	1.3	1	300
e-Au	30	2	1	100
r-Au	15	2	1	100

Table 1: Values of the parameters obtained through the best fit procedure of the experimental data shown in Figure 28.

As suggested by the sampling in size, we choose a simple analytical function of the log-normal [4] type:

$$n(r) \propto r^{-1} \exp\left[-\frac{(\ln r - \ln r_m)^2}{2(\ln \sigma_m)^2}\right] \tag{34}$$

to fit the experimental data. In the present simulations, the optical constants for both an Au NP and an Ag NP are those derived from the work of Johnson and Christy [93].

The results of the theoretical analysis are plotted together with the experimental spectra in Figure 28a,b for Ag NPs before and after the laser re-irradiation and in Figure 28c,d for Au NPs. From Figure 28 and Table 1, where we report the best fit parameters obtained with the above described theoretical procedure, we notice that the further fragmentation of the elemental NPs due to re-irradiation is confirmed by the accuracy of our theoretical computation. Overall, our theoretical approach is in agreement with the experimental data for all elemental samples.

5.2 Simulations of the UV-Vis spectra for mixtures of the elemental colloids

In Figure 29, we show the comparison between the Uv-Vis spectra for the colloids of the equiatomic m-$Ag_{50}Au_{50}$ mixture and of their re-irradiated counterparts, r-$Ag_{50}Au_{50}$. The first curve (blue line, labelled m-$Ag_{50}Au_{50}$) displays two peaks, one centered at about 398 nm (FWHM 48 nm), due to e-Ag NPs, the second at 511 nm (FWHM 35 nm), due to e-Au NPs. Even if the shape of both peaks indicates the presence of isolated, spherical NPs, the mixed sample shows new features as compared to the extinction spectra of the colloids in Figure 28. The SPR peaks are shifted towards lower wavelengths: from 407 nm to 398 nm for e-Ag and from 526 nm to 511 nm for e-Au. Peaks are also narrower: the FWHM changes from 70 nm to 48 nm for e-Ag, and from 80 nm to 35 nm for e-Au. This led us to theoretically analyze the spectra of purely mixed samples to understand the nature of the above changes. The spectrum of the re-irradiated colloids (red line labelled r-$Ag_{50}Au_{50}$ in Figure 29), consists of a *single* peak centered at 504 nm (FWHM 52 nm). Thus the optical signal from Ag NPs disappeared, and the one from Au NPs is blue-shifted and broadened, lying between those of e-Ag and e-Au [94, 95]. Its displacement toward the Au feature is likely to indicate that the composition of the NPs is enriched in Au, similarly to what was reported in references [94, 95]. The result of the re-irradiation indicates that the NPs underwent a drastic change leading to the formation of a nano-alloy [96, 97, 98].

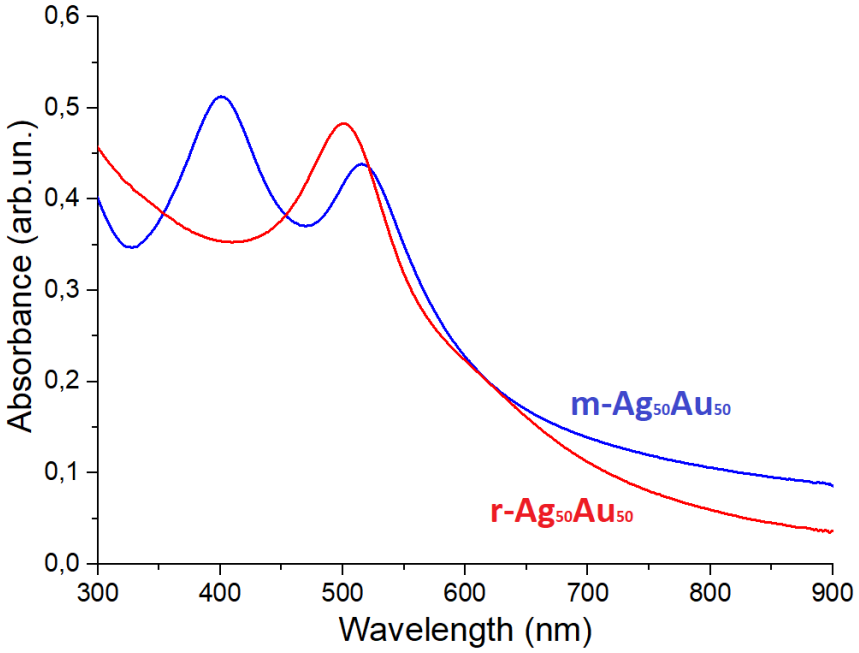

Figure 29: Extinction spectra of: the initial $Ag_{50}Au_{50}$ equiatomic physical mixture (m-Ag_{50} Au_{50}) of the as-prepared colloids, blue line, and the re-irradiated colloids (r-$Ag_{50}Au_{50}$), red line. Notice that the two features due to Ag and Au isolated, spherical NPs in m-$Ag_{50}Au_{50}$ reduce to a single feature in r-$Ag_{50}Au_{50}$, blue-shifted with respect to the SPR of the initial e-Au colloid.

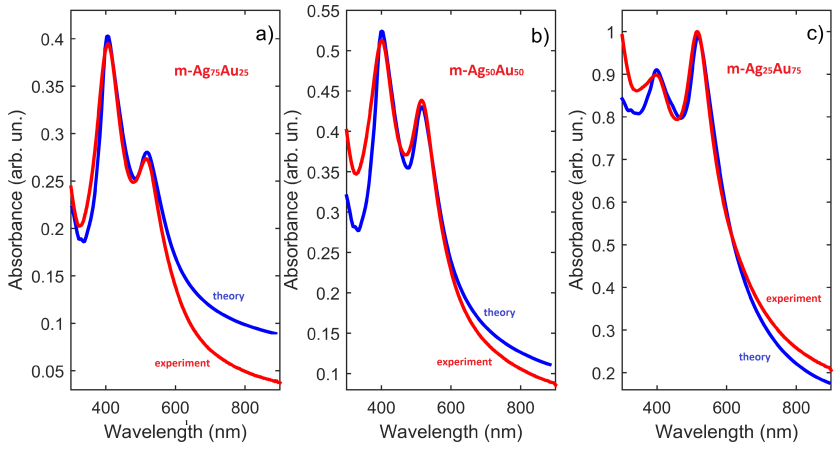

Figure 30: Extinction spectra from the experiment (red line) and simulation (blue line) for three m-Ag_xAu_{100-x} mixed colloids of different stoichiometry, spanning the composition range: m-$Ag_{75}Au_{25}$ (a); m-$Ag_{50}Au_{50}$ (b); m-$Ag_{25}Au_{75}$ (c).

In Figure 30, we report the UV-Vis and the simulated extinction spectra of m-Ag_xAu_{100-x} colloids for selected x values. The reported simulations make use of information on the average NP size as in Table 1.

Here we notice further effects: (1) the relative intensity of the peak at about 400 nm, associated to Ag NPs, increases on increasing Ag content, (2) the Ag peak undergoes a gradual red shift from 398 nm to 406 nm, (3) the Au NP feature shifts progressively from 515 nm to 507 nm on lowering the Au content. This is further confirmation that the surface plasmon characteristics of Ag and Au colloids strongly depend on the stoichiometric ratio of the mixture [96, 94]. Electron microscopy images show that in the Au-Ag mixtures, the NPs have a tendency to join together (see Figure 27a).

The observed shifts can be theoretically justified by supposing that, upon mixing, there is a weak interaction, due to nanoscale forces mainly of electrostatic nature [99], between the particles that make up the mixture. This interaction also studied from the experimental point of view [96], is related to the high activity of Ag NPs that has been shown to depend on the wavelength of the laser radiation used in the synthesis [96]. Moreover, the change in the broadening of the plasmon band compared with that obtained for elemental colloids indicates the collective nature of the SPR of the mixed sample[100]. In the simulation, we focused on the electromagnetic interaction via the multiple scattering effects that come into play in the mixed sample. To take into account these effects, we calculate the optical properties (σ_{ext}) through the T-matrix approach, referring to the simplest form of aggregation: a dimer consisting of an Ag sphere and an Au sphere. By varying the distance between the monomers that make up such a binary system and by mediating over all the possible orientations, it was possible to take into account such shifts that are a fingerprint of multiple scattering interactions between the monomers that constitute the dimer.

5.3 Simulations of the UV-Vis spectra for re-irradiated mixtures of elemental colloids

Here we present the simulations obtained for the re-irradiated samples made by mixing e-Au and e-Ag colloids, where the Ag fraction ranges from 25% to 75%. From the analysis of the experimental data (see Figure 29 for the equiatomic composition case), we observe the disappearance of the lowest frequency peak, which we previously

assigned to Ag NPs. The question that arises is which chemical-physical process is responsible for this behavior. The experiment demonstrates, in agreement with assessed literature [94, 95], that after the re-irradiation, particles with different optical properties to those of e-NPs were formed. We aim to demonstrate that our theoretical approach can discriminate whether such particles are:

(1) core-shell NPs;

(2) NPs with optical properties that can be derived in terms of an effective dielectric constant following Bruggeman effective medium approximation (EMA) [83];

(3) a new kind of NPs, the optical properties of which can be simulated assuming that re-irradiation led to the formation of Ag-Au alloys. In this case, we consider two different models for the dielectric constant: the model of Rioux et al [101], which we refer as *analytic model*, and the model of Pena-Rodriguez et al. [102].

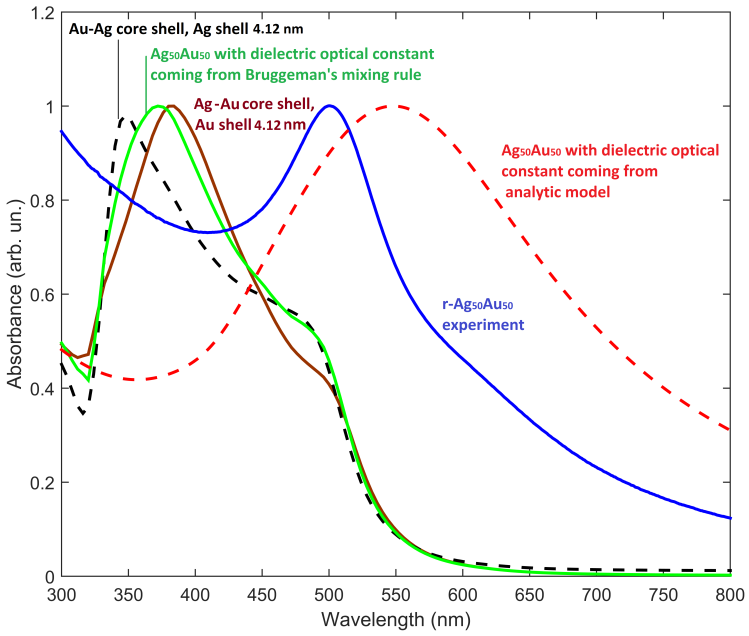

Figure 31: Extinction spectra for $Ag_{50}Au_{50}$, from different models: Au-Ag core-shell, Au shell, 4.12 nm (red line); Au-Ag core-shell, Ag shell, 4.12 nm (black dashed line); $Ag_{50}Au_{50}$ with the dielectric optical constant coming from Bruggeman's mixing rule (green line); $Ag_{50}Au_{50}$ with the dielectric optical constant coming from analytic model [101] (red dashed line); the blue line refers to experimental extinction spectrum of r-$Ag_{50}Au_{50}$ colloids.

In Figure 31 we present the computed normalized absorption for different nanospheres with diameter $r = 20$ nm, compared with the experimental spectrum for the colloid r-$Ag_{50}Au_{50}$.

The curves are obtained for a core-shell spherical NP for homogeneous spheres using both Bruggeman's EMA (Effective Medium Approximation) and dielectric optical constant coming from the analytic model [101]. The core-shell NP is constituted by a shell, the volume of which is 50% of the total volume, and we consider both the case of Au-core with Ag-shell and Ag-core with Au-shell. In the

simulation, we adopted for Ag and Au the Johnson and Christy dielectric constants [93]. The Bruggeman's effective dielectric constant is derived for a mixture of 50% Ag and 50% Au. In Figure 31 we notice that the absorption spectra for the three above models (red and black dashed curves, green curve, and red dashed curve) are very far from the experimental data. As expected, in the first case, the layered structure introduces a further peak due to the presence of the core that marks the optical behavior. Bruggeman's model gives an absorption spectrum with a behavior that is, as expected, an intermediate result between those of the two core-shell spectra. Also, the result obtained by Rioux's analytic model (red dashed curve) presented in Figure 31 is far from the experimental data. All such unsatisfactory results indicate that the re-irradiation of the sample results in colloids made of NPs with optical properties that can no longer be described through the dielectric functions that make use of a mixing rule based on Johnson and Christy results or on a multi-parametric modification of Drude-Lorentz model. Indeed, any mixing rule ultimately tends to preserve the main physical characteristics of the noble metals used in the experiment. For these reasons, we resort to the optical constants for real Ag-Au alloys obtained from spectroscopic ellipsometry measurements on thin films fabricated by electron beam evaporation [102]. The ellipsometric spectra of thin films of Ag-Au alloys with different compositions were analyzed by an analytical procedure based on Kramers-Kronig (K-K) compliant cubic B-splines [103], this way ensuring the physical meaning of the obtained complex dielectric function. A three-phase multilayer model was assumed in which the second layer, modeled as a Bruggeman's mixture of voids and Ag-Au islands, simulates the film surface with its roughness,

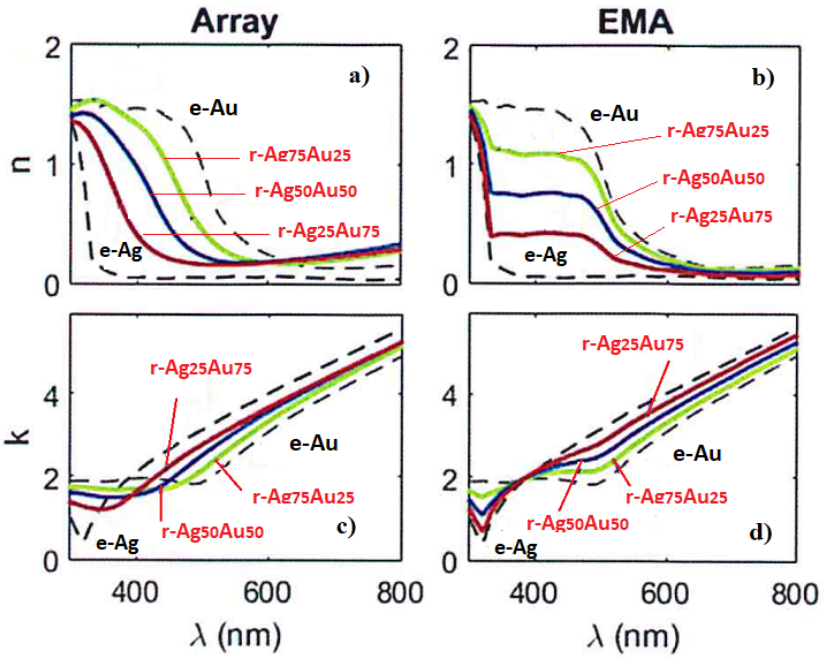

Figure 32: Real (n, panel a) and imaginary (κ, panel c) parts of the refractive index as functions of the wavelength for re-irradiated r-Ag-Au colloids of different composition: red line r-$Ag_{25}Au_{75}$; blue line r-$Ag_{50}Au_{50}$; green line $Ag_{75}Ag_{25}$; data for pure Ag and Au (e-Ag and e-Au) are reported. In panels b and d, the same as in panels a and c, calculated from Bruggeman's mixing rule.

lying between the ambient and the high-density region of the alloy film [102]. In Figure 32a and 32c, we display the values of the real (n) and imaginary (κ) parts of the refractive index corresponding to the r-Ag-Au alloys we prepared re-irradiating colloid mixtures containing (i) 25%Ag-75%Au (red line), (ii) 50%Ag-50%Au (blue line) and (iii) 75%Ag-25%Au (green line) together with the real and imaginary parts of the refractive index of the pure noble metals [93]. For comparison, in Figure 32b and 32d, we show the values of n and κ obtained with Bruggeman's mixing rule for the same systems.

We remark a couple of peculiarities in the trend of the refractive index as a

function of the wavelength as the composition changes: first, for the alloy, the onset of interband transitions shifts significantly from ≈500 nm in pure Au to ≈315 nm for pure Ag unlike what happens for the mixing rule; and second, in the near IR region for the alloy there is a non-linear behavior in the real part of the refractive index that leads to values of n larger than those for pure metals. The physical reason for the presence of this shift is the variation of the number density of the minority constituent of the material. Since such atoms act as scattering centers, a variation in the resistivity of the material and, ultimately, in the damping constant is induced. The damping constant reaches its maximum value for the composition Ag 50% - Au 50% [104]. The non-linear behavior at near IR is caused by the difference in electronegativity between Ag and Au, resulting in a considerable transfer of electronic density from Ag to Au. This charge transfer stresses and modifies the lattice, producing additional damping.

In Figure 33, we report the normalized experimental UV-Vis absorbance in good agreement with the calculated values for the re-irradiated mixtures with different compositions. For the simulated absorbance, we adopted the previously discussed model for the dielectric constant of the alloy and, also in this case, we considered a log-normal distribution in size (see Eqs. 33, 34). In Table 2, we report the parameters obtained in the best-fit procedure. We underline that, as a secondary effect of the re-irradiation procedure, the obtained colloids undergo a further NP fragmentation so that a narrower size distribution results as compared to that used for the best fit of Figure 28.

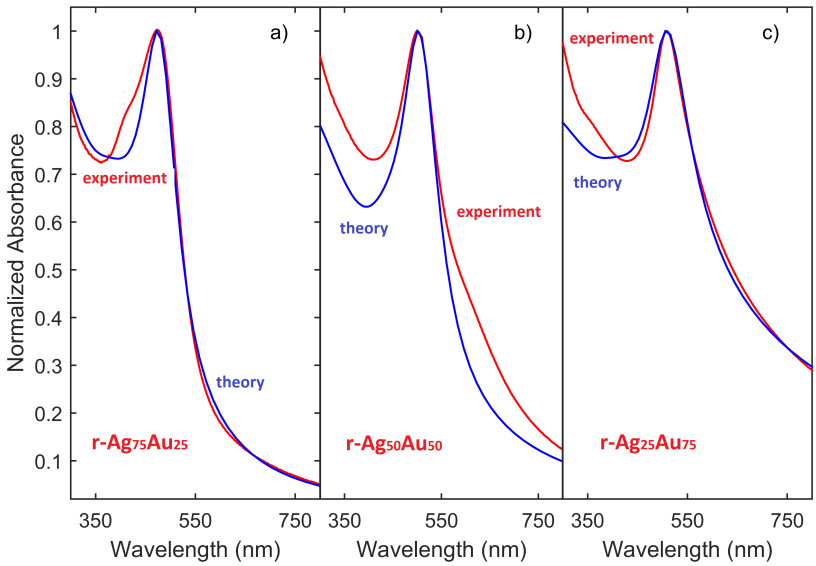

Figure 33: Experimental (red line) and calculated (blue line) normalized extinction spectra of re-irradiated colloids of different composition: r-$Ag_{75}Au_{25}$ (a); r-$Ag_{50}Au_{50}$ (b); r-$Ag_{75}Ag_{25}$ (c).

	r_{av} (nm)	σ	r_{min} (nm)	r_{max} (nm)
25%Au-75%Ag	10	2	1	100
50%Au-50%Ag	10	2	1	100
75%Au-25%Ag	10	2.5	1	100

Table 2: Values of the parameters obtained through the best-fit procedure of the experimental data are shown in Figure 33.

Conclusions

This thesis discusses some of the most used analytical and numerical approaches to address the scattering problem. The choice of the best method to use is crucial for the solution of the problem and depends on the composition and morphology of the system under study, on the wavelength range under investigation, on the desired level of accuracy, and on the available computational resources. Throughout this thesis we compare the potentials of an analytical and numerical approach based on the multipole field expansion of the electromagnetic fields, namely the T-matrix method, with numerical approaches based on finite elements methods, specifically the FDTD method. In some situations also the use of approximate approaches may give a useful insight into the physics of light scattering. For this reason we also discuss the dipole approximation and the scattering regime in which it can be reasonably applied.

A throughout discussion is devoted to the theory of optical trapping and optical tweezers which in recent years have found relevant applications in many fields, from biology to soft matter, ultra-sensitive spectroscopy, atomic physics, nanophotonics, and nanomedicine [9]. Also in this case we compare the potential of T-matrix, FDTD and dipole approximation for calculating optical forces, showing a numerical comparison between the different approaches.

In recent years optical tweezers have found application to study dust particles of astrophysical interest and to characterize their opto-mechanical behaviour (space

tweezers) [11]. The study of cosmic dust, in the form of interstellar, interplanetary, and planetary dust particles has gained much relevance in the last decades since it has been finally recognized its crucial role in many processes, going from planet and star formation to the ignition of a potentially life-bearing chemistry. We show how the T-matrix method can be applied to model and calculate the optical forces acting on cosmic dust analogues, highlighting the key role played by dust composition and morphology for optical trapping. This study provides significant insights into the potential applications of optical tweezers for analyzing particulate matter in the solar system. The techniques explored in this research could be extended to the study of cometary particles, including their volatile components, as well as dust particles in the Martian atmosphere and on the surfaces of both Mars and the Moon. Such applications could be crucial for "clean" handling and preliminary characterization of planetary particulate matter in curation facilities, paving the way for future space exploration and in-situ analysis of planetary bodies [6].

Finally, we present some simulations related to the UV-Vis optical response of Ag-Au colloidal solutions obtained through laser ablation with specific control parameters. To accomplish this, we utilize the T-matrix approach developing a theoretical model based on the Mie theory to explain the experimental observations, taking into account the core-shell structure of the nanoparticles and the interaction between the plasmon resonances of Ag and Au. Our model predicts the position and intensity of the plasmon peaks as a function of the molar ratio of Ag to Au, which is consistent with the experimental data. Our study provides insights into the optical properties of Ag-Au colloidal alloys and their potential applications in

nanotechnology. Our theoretical analysis contributes to a better understanding of the underlying physical mechanisms that govern the optical properties of these materials [12]. Further research could explore the effects of other variables, such as particle size and shape, on the optical properties of Ag-Au colloidal alloys and could investigate the use of other theoretical models to describe their behavior.

Acknowledgment

A special thanks to Prof. Rosalba SAIJA as a great mentor and supervisor. Her advice, guidance, patience, and insight made this thesis possible. I am forever grateful for everything you have done for me. “Thank you for believing in me and always making time for me. This thesis is a reflection of your invaluable contributions to my academic and personal growth. Thank you for everything”.

I wish to express my deepest gratitude to Dr. Maria Antonia IATÌ, that has dedicated her time and effort in providing assistance. To Dr. Onofrio M. MARAGÒ and to Dr. Maria Grazia DONATO for their invaluable guidance and support throughout this thesis. “Thank you for your dedication and collaboration”. To mention thank you also to Dr. Pablo ALBELLA for providing a wonderful opportunity to do research at the University of Cantabria.

I am indebted to both of my parents, Ahmed SAIDI and Saida SWALMI have always been there to support me from the start and whose unwavering support, encouragement, and sacrifices. “You have always believed in me, pushed me to be my best, and have been my biggest cheerleaders throughout this academic journey. Your love, guidance, and sacrifices have been my constant source of strength and inspiration. I cannot express in words how grateful I am to have you as my parents. This thesis is a tribute to your love and dedication to my education. Thank you for

everything, I love you both".

To my dear sisters, Souha SAIDI, Manar SAIDI, and the little beautiful Imen SAIDI, are a huge inspiration for me in every single way. and I am grateful for your presence in my life. This thesis is dedicated to you for your friendship, love, and unwavering support. "Thank you for always being there for me".

To all my dear friends, they have been a constant source of joy, laughter, and support throughout my academic journey. Your unwavering friendship and support have been the highlight of my academic journey.

References

[1] P. H. Jones, O. M. Maragò, and G. Volpe, *Optical tweezers: Principles and applications*. Cambridge: Cambridge University Press, 2015.

[2] M. G., "Beiträge zur optik trüber medien, speziell kolloidaler metallösungen," *Ann. Phys.*, vol. 330, pp. 377–445, 1908.

[3] AA.VV., *The Mie Theory.Basics and Applications*. W. Hergert, T. Wriedt Eds.: Springer Series in Optical Sciences (SSOS, volume 169), 2012.

[4] M. Mishchenko, L. Travis, and A. Lacis, *Scattering, absorption, and emission of light by small particles*. Cambridge University Press, 2002.

[5] P. C. Waterman, "Symmetry, unitarity, and geometry in electromagnetic scattering," *Physical Review D*, vol. 3, pp. 825–839, 1971.

[6] A. Magazzù, D. B. Ciriza, A. Musolino, A. Saidi, P. Polimeno, M. G. Donato, A. Foti, P. G. Gucciardi, M. A. Iatì, R. Saija, N. Perchiazzi, A. Rotundi, L. Folco, and O. M. Maragò, "Investigation of dust grains by optical tweezers for space applications," *The Astrophysical Journal*, vol. 942, no. 11, 2023.

[7] B. Fazio, P. Artoni, M. Antonia Iatì, C. D'andrea, M. J. Lo Faro, S. Del Sorbo, S. Pirotta, P. Giuseppe Gucciardi, P. Musumeci, C. Salvatore Vasi, *et al.*, "Strongly enhanced light trapping in a two-dimensional silicon nanowire random fractal array," *Light: Science & Applications*, vol. 5, no. 4, pp. e16062–e16062, 2016.

[8] G. Pesce, P. H. Jones, O. M. Maragò, and G. Volpe, "Optical tweezers: theory and practice," *The European Physical Journal Plus*, vol. 135, pp. 1–38, 2020.

[9] G. Volpe and *et al.*, "Roadmap for optical tweezers 2023," *J. Phys. Photonics*, vol. 5, p. 022501, 2023.

[10] D. Jackson, *Classical electrodynamics*. Wiley, New York, 2nd ed., 1975.

[11] P. Polimeno and al., "Optical tweezers in a dusty universe," *The European Physical Journal Plus*, vol. 136, no. 339, 2021.

[12] E. e. a. Fazio, "On the optical properties of ag-au colloidal alloys pulsed laser ablated in liquid: Experiments and theory," *Journal of Physical Chemistry C*, vol. 124, pp. 24930–24939, 2020.

[13] F. Borghese, P. Denti, and R. Saija, *Scattering from Model Nonspherical Particles*. Berlin: Springer, 2007.

[14] W. J. Wiscombe, *Mie scattering calculations: Advances in technique and fast, vector-speed computer codes*, vol. 10. National Technical Information Service, US Department of Commerce, 1979.

[15] F. Borghese, P. Denti, R. Saija, and M. A. Iatì, "Optical trapping of nonspherical particles in the T-matrix formalism," *Opt. Express*, vol. 15, pp. 11984–11998, 2007.

[16] D. Van de Hulst, *Light scattering by small particles*. ***: Dover Publications, New York, 1957.

[17] F. Borghese, P. Denti, R. Saija, G. Toscano, and O. Sindoni, "Extinction coefficients for a random dispersion of small stratified spheres and a random dispersion of their binary aggregates," *J. Opt. Soc. Am. A*, vol. 4, pp. 1984–1991, 1987.

[18] J. H. Bruning and Y. T. Lo, "Multiple scattering of em waves by spheres. i.multipole expansion and ray-optical solution," *IEEE Trans. Antennas Propag.*, vol. 19, pp. 391–400, 1971.

[19] B. Peterson and S. Strom, "T-matrix for electromagnetic scattering from an arbitrary number of scatterers and representations of e(3)," *Phys. Rev. D*, vol. 8, pp. 3661–3678, 1973.

[20] J. M. Gerardy and M. Ausloos, "Absorption spectrum of clusters of spheres from the general solution of maxwell's equations," *Phys. Rev. B*, vol. 22, pp. 4950–4959, 1980.

[21] F. Borghese, P. Denti, R. Saija, G. Toscano, and O. I. Sindoni, "Scattering from multilayered spheres: comparison of mie theory and a superposition t-matrix method," *Appl. Opt.*, vol. 23, no. 15, pp. 2502–2506, 1984.

[22] F. Borghese, P. Denti, G. Toscano, and O. Sindoni, "An addition theorem for vector helmholtz harmonics," *Journal of Mathematical Physics*, vol. 21, no. 12, pp. 2754–2755, 1980.

[23] J. P. Gordon, "Radiation forces and momenta in dielectric media," *Physical Review A*, vol. 8, p. 14, 1973.

[24] E. M. Purcell and C. R. Pennypacker, "Scattering and absorption of light by nonspherical dielectric grains," *The Astrophysical Journal*, vol. 186, pp. 705––714, 1973.

[25] V. Amendola, R. Pilot, M. Frasconi, O. M. Maragò, and M. A. Iatì, "Surface plasmon resonance in gold nanoparticles: a review," *Journal of Physics: Condensed Matter*, vol. 29, no. 20, p. 203002, 2017.

[26] B. T. Draine and J. Goodman, "Beyond clausius-mossotti -wave propagation on a polarizable point lattice and the discrete dipole approximation," *The Astrophysical Journal*, vol. 405, pp. 685—-697, 1993.

[27] F. M. Kahnert, "Numerical methods in electromagnetic scattering theory," *Journal of Quantitative Spectroscopy Radiative Transfer*, vol. 79–80, pp. 775–824, 2003.

[28] S. K. Yee, "Numerical solution of initial boundary value problems involving maxwell's equations in isotropic media.," *IEEE Trans. Antennas Propag.*, vol. 14, pp. 302–307, 1966.

[29] T. L. Civita, *Caratteristiche dei sistemi differenziali e propagazione ondosa*. Zanichelli, Bologna, 1992.

[30] M. Fusco, "Fdtd algorithm in curvilinear coordinates (em scattering)," *IEEE Transactions on Antennas and Propagation*, vol. 38, pp. 76–89, 1990.

[31] K. S. K. L. Simpson, "A technique for increasing the resolution of finite-difference solutions of the maxwell equation," *IEEE Transactions on Electromagnetic Compatibility*, vol. EMC-23, no. 4, pp. 419–422, 1981.

[32] J. Cole, "A high accuracy fdtd algorithm to solve microwave propagation and scattering problems on a coarse grid," *IEEE Transactions on Microwave Theory and Techniques*, vol. 43, pp. 2053–2058, 1995.

[33] P. Yang and K. N. Liou, "Light scattering by hexagonal ice crystals: comparison of finite-difference time domain and geometric optics models," *Journal of the Optical Society of America A*, vol. 12, pp. 162–176, 1995.

[34] K. U. A. Taflove, "A novel method to analyze electromagnetic scattering of complex objects," *IEEE Transactions on Electromagnetic Compatibility*, vol. EMC-24, pp. 397–405, 1982.

[35] P. Yang and K. N. Liou, "Geometric-optics–integral-equation method for light scattering by nonspherical ice crystals," *Applied Optics*, vol. 35, pp. 6568–6584, 1996.

[36] K. Yee, "Numerical solution of initial boundary value problems involving maxwell's equations in isotropic media," *IEEE Transactions on Antennas and Propagation*, vol. 14, pp. 302–307, 1966.

[37] M. B. A Taflove, "Numerical solution of steady-state electromagnetic scattering problems using the time-dependent maxwell's equations," *IEEE Trans. Microwave Theory and Tech.*, vol. 23, pp. 623–630, 1975.

[38] M. E. B. A. Taflove, "Numerical solution of steady-state electromagnetic scattering problems using the time-dependent maxwell's equations," *IEEE Transactions on Microwave Theory and Techniques*, vol. 23, pp. 623– 630, 1975.

[39] G. Mur, "Difference approximation of the time-domain electromagnetic-field equations," *IEEE Transactions on Electromagnetic Compatibility*, vol. 23, pp. 377 – 382, 1981.

[40] F. Borghese, P. Denti, R. Saija, M. A. Iatì, and O. M. Maragó, "Radiation torque and force on optically trapped linear nanostructures," *Phys. Rev. Lett.*, vol. 100, p. 163903, 2008.

[41] M. I. Mishchenko, "Radiation force caused by scattering, absorption, and emission of light by nonspherical particles," *J. Quant. Spectrosc. Radiat. Transfer*, vol. 70, pp. 811–816, 2001.

[42] R. Saija, M. A. Iatí, A. Giusto, P. Denti, and F. Borghese, "Transverse components of the radiation force on nonspherical particles in the T-matrix formalism," *J. Quant. Spectrosc. Radiat. Transf.*, vol. 94, pp. 163 – 179, 2005.

[43] F. Borghese, P. Denti, R. Saija, and M. A. Iatì, "Optical trapping of nonspherical particles in the T-matrix formalism," *Opt. Express*, vol. 15, no. 19, pp. 11984–11998, 2007.

[44] B. Richards and E. Wolf, "Electromagnetic diffraction in optical systems. ii. structure of the image field in an aplanatic system," *Proc. Roy. Soc. London A*, vol. 8, no. 253, pp. 358–379, 1959.

[45] L. Novotny and B. Hecht, *Principles of Nano-Optics*. Cambridge: Cambridge University Press, 2008.

[46] O. M. Maragò, P. H. Jones, F. Bonaccorso, V. Scardaci, P. G. Gucciardi, A. G. Rozhin, and A. C. Ferrari, "Femtonewton force sensing with optically trapped nanotubes," *Nano Lett.*, vol. 8, pp. 3211–3216, 2008.

[47] O. Maragò, P. Gucciardi, and P. Jones, "Photonic force microscopy: from femtonewton force sensing to ultra-sensitive spectroscopy," in *Scanning Probe Microscopy in Nanoscience and Nanotechnology*, pp. 23–56, Springer, 2010.

[48] M. Mansuripur, "Distribution of light at and near the focus of high-numerical-aperture objectives," *J. Opt. Soc. Am. A*, vol. 3, pp. 2086–2093, 1986.

[49] M. Mansuripur, "Certain computational aspects of vector diffraction problems," *J. Opt. Soc. Am. A*, vol. 6, no. 253, pp. 786–805, 1989.

[50] M. Mansuripur, "Distribution of light at and near the focus of high-numerical-aperture objectives: erratum, certain computational aspects of vector diffraction problems: erratum," *J. Opt. Soc. Am. A*, vol. 10, pp. 382–383, 1993.

[51] F. Borghese, P. Denti, R. Saija, and M. A. Iatì, "Radiation torque on nonspherical particles in the transition matrix formalism," *Optics Express*, vol. 14, pp. 9508–9521, 2006.

[52] F. Calura, A. Pipino, and F. Matteucci, "The cycle of interstellar dust in galaxies of different morphological types," *Astronomy & Astrophysics*, vol. 479, pp. 669–685, 2008.

[53] S. E. Woosley, A. Heger, and T. A. Weaver, "The evolution and explosion of massive stars," *Reviews of Modern Physics*, vol. 74, pp. 1015–1071, 2002.

[54] S. Woosley and T. A. Weaver, "The evolution and explosion of massive stars ii: Explosive hydrodynamics and nucleosynthesis," *Tech. Rep. (Lawrence Livermore National Lab., CA (United States)*, 1995.

[55] F. J. Rietmeijer, "Interplanetary dust particles," *Planetary Materials*, vol. 36, 1998.

[56] A. J. Westphal *et al.*, "Evidence for interstellar origin of seven dust particles collected by the stardust spacecraft," *Science*, vol. 345, pp. 786–791, 2014.

[57] D. Brownlee *et al.*, "Stardust: Comet and interstellar dust sample return mission," *Journal of Geophysical Research: Planets*, vol. 108, no. E12, p. 8111, 2003.

[58] D. R. Frank *et al.*, "Stardust interstellar preliminary examination ii: Curating the interstellar dust collector, picokeystones, and sources of impact tracks," *Meteoritics & Planetary Science*, vol. 49, no. 12, pp. 2276–2315, 2014.

[59] J. P. Testa *et al.*, "Collection of microparticles at high balloon altitudes in the stratosphere," *Earth and Planetary Science Letters*, vol. 98, pp. 287–302, 1990.

[60] V. D. Corte *et al.*, "In situ collection of refractory dust in the upper stratosphere: The duster facility," *Space Science Reviews*, vol. 169, no. 1-4, pp. 149–176, 2012.

[61] M. J. Genge, C. Engrand, M. Gounelle, and S. Taylor, "The classification of micrometeorites," *Meteoritics & Planetary Science*, vol. 43, no. 3, pp. 497–515, 2008.

[62] F. J. Rietmeijer, "Identification of fe-rich meteoric dust," *Planetary and Space Science*, vol. 49, p. 71–77, 2001.

[63] P. Stysley, "Laser-based optical trap for remote sampling of interplanetary and atmospheric particulate matter," *Technical report, NASA*, 2014.

[64] A. Rotundi and al., "Combined micro-raman, micro-infrared, and field emission scanning electron microscope analyses of comet 81p/wild 2 particles collected by stardust," *Meteoritics & Planetary Science*, vol. 43, pp. 367–397, 2008.

[65] A. Rotundi and al., "Two refractory wild 2 terminal particles from a carrot-shaped track characterized combining mir/fir/raman microspectroscopy and fe-sem/eds analyses," *Meteoritics & Planetary Science*, vol. 49, pp. 550–575, 2014.

[66] A. E. Rubin and J. N. Grossman., "Meteorite and meteoroid: New comprehensive definitions.," *Meteoritics Planetary Science*, vol. 45, pp. 114–122, 2010.

[67] D. Nesvorny, D. Vokrouhlicky, W. F. Bottke, and M. Sykes, "Physical properties of asteroid dust bands and their sources," *Icarus*, vol. 181, pp. 107–144, 2006.

[68] G. J. Flynn, J. M. Cordfunke, J. Borg, B. Zanda, S. Mostefaoui, and D. E. Brownlee, "Dust production from the hypervelocity impact disruption of the murchison hydrous cm2 meteorite: Implications for the disruption of hydrous asteroids and the production of interplanetary dust," *Planetary and Space Science*, vol. 57, pp. 119–126, 2009.

[69] M. Fulle, A. Rotundi, V. D. Corte, G. Rinaldi, R. Sordini, L. Colangeli, J. Agarwal, E. M. Epifani, M. Hilchenbach, I. Bertini, F. Ferri, and A. Weissman, "How comets work: Nucleus erosion versus dehydration," *Monthly Notices of the Royal Astronomical Society*, vol. 493, pp. 4039–4044, 2020.

[70] C. Guttler, C. Koenders, J.-B. Vincent, S. F. Hviid, E. Kuhrt, L. M. Lara, S. Merouane, O. Poch, J. D. C. Sánchez, S. Faggi, S. Fornasier, H. U. Keller, M. Massironi, S. Mottola, G. Naletto, and C. Tubiana, "Synthesis of the morphological description of cometary dust at comet 67p/churyumov-gerasimenko," *Astronomy & Astrophysics*, vol. 630, p. A24, 2019.

[71] C. Cordierand and L. Folco., "Oxygen isotopes in cosmic spherules and the composition of the near earth interplanetary dust complex.," *Geochimica et Cosmochimica Acta*, vol. 146, pp. 18–26, 2014.

[72] M. D. Suttle and L. Folco., "The extraterrestrial dust fux: Size distribution and mass contribution estimates inferred from the transantarctic mountains (tam) micrometeorite collection.," *Journal of Geophysical Research: Planets*, vol. 125, p. e2019JE006241, 2020.

[73] V. D. Corte and al., "In situ collection of refractory dust in the upper stratosphere: the duster facility.," *Space Science Reviews*, vol. 169, pp. 159–180, 2012.

[74] F. J. Rietmeijer., "The earliest chemical dust evolution in the solar nebula.," *Geochemistry*, vol. 62, pp. 1–45, 2002.

[75] V. D. Corte and al., "67p/cg inner coma dust properties from 2.2 au inbound to 2.0 au outbound to the sun.," *Monthly Notices of the Royal Astronomical Society*, vol. 462, pp. S210–S219, 2016.

[76] A. Rotundi, H. Sierks, and et al., "Dust measurements in the coma of comet 67p/churyumov-gerasimenko inbound to the sun.," *Science*, vol. 347, p. 6220, 2015.

[77] F. J. M. Rietmeijer, V. Della Corte, M. Ferrari, A. Rotundi, and R. Brunetto, "Laboratory analyses of meteoric debris in the upper stratosphere from settling bolide dust clouds," *Icarus*, vol. 266, pp. 217–234, 2016.

[78] F. Oliva, E. D'Aversa, G. Liberti, G. Sindoni, F. Altieri, and E. Castelli, "A database of aerosols and gases coefficients for vis-nir radiative transfer in the solar system planetary atmospheres," *Planetary and Space Science*, vol. 166, pp. 101–109, 2019.

[79] A. Rotundi, F. Rietmeijer, M. Ferrari, V. Della Corte, G. Baratta, R. Brunetto, E. Dartois, Z. Djouadi, S. Merouane, J. Borg, *et al.*, "Two refractory wild 2 terminal particles from a carrot-shaped track characterized combining mir/fir/raman microspectroscopy and fe-sem/eds analyses," *Meteoritics & Planetary Science*, vol. 49, no. 4, pp. 550–575, 2014.

[80] W. G. Egan and T. Hilgeman, "Optical constants for terrestrial analogs of lunar materials," *The Astronomical Journal*, vol. 78, p. 799, 1973.

[81] F. Rietmeijer and al., "Laboratory analyses of meteoric debris in the upper stratosphere from settling bolide dust clouds," *Icarus*, vol. 266, p. 217–234, 2016.

[82] A. Collareta, M. D'Orazio, M. Gemelli, A. Pack, and L. Folco, "High crustal diversity preserved in the lunar meteorite mount dewitt 12007 (victoria land, antarctica)," *Meteoritics & Planetary Science*, vol. 51, no. 2, pp. 351–371, 2016.

[83] D. E. Aspnes, J. B. Theeten, and F. Hottier, "Investigation of effective-medium models of microscopic surface roughness by spectroscopic ellipsometry," *Phys. Rev. B*, vol. 20, pp. 3292–3302, oct 1979.

[84] A. E. Rubin and J. N. Grossman., "Meteorite and meteoroid: New comprehensive definitions.," *Meteoritics Planetary Science*, vol. 45, pp. 114–122, 2020.

[85] B. Draine and H. M. Lee, "Optical properties of interstellar graphite and silicate grains.," *The Astrophysical Journal*, vol. 285, pp. 89–108, 1984.

[86] A. Gwynn, "Late medieval irish literary tradition," *Proceedings of the Royal Irish Academy. Section C: Archaeology, Celtic Studies, History, Linguistics, Literature*, vol. 74, pp. 1–39, 1974.

[87] S. Nakazawa, "Thermodynamic properties of water in the earth's mantle," *Geochimica et Cosmochimica Acta*, vol. 41, no. 7, pp. 945–951, 1977.

[88] J. Dorschner, B. Begemann, T. Henning, C. Jaeger, H. Mutschke, R. Nass, and E. Thamm, "Steps toward interstellar silicate mineralogy. ii. study of mg-fe-silicate glasses of variable composition," *Astronomy and Astrophysics*, vol. 300, p. 503, 1995.

[89] X. Wang, "Properties and applications of silicon nanowires," *Materials Science in Semiconductor Processing*, vol. 40, pp. 585–597, 2015.

[90] A. Letzel, M. Santoro, J. Frohleiks, A. R. Ziefuß, S. Reich, A. Plech, E. Fazio, F. Neri, S. Barcikowski, and B. Gökce, "How the re-irradiation of a single ablation spot affects cavitation bubble dynamics and nanoparticles properties in laser ablation in liquids," *Applied Surface Science*, vol. 473, pp. 828–837, 2019.

[91] T. Hupfeld, F. Stein, S. Barcikowski, B. Gökce, and U. Wiedwald, "Manipulation of the Size and Phase Composition of Yttrium Iron Garnet Nanoparticles by Pulsed Laser Post-Processing in Liquid," *Molecules*, vol. 25, p. 1869, apr 2020.

[92] A. R. Ziefuß, S. Reichenberger, C. Rehbock, I. Chakraborty, M. Gharib, W. J. Parak, and S. Barcikowski, "Laser fragmentation of colloidal gold nanoparticles with high-intensity nanosecond pulses is driven by a single-step fragmentation mechanism with a defined educt particle-size threshold," *The Journal of Physical Chemistry C*, vol. 122, no. 38, pp. 22125–22136, 2018.

[93] P. Johnson and R. Christy, "Optical Constants of the Noble Metals," *Physical Review B*, vol. 6, pp. 4370–4379, dec 1972.

[94] F. Hajiesmaeilbaigi and A. Motamedi, "Synthesis of Au/Ag Alloy nanoparticles by Nd: YAG laser irradiation," *Laser Physics Letters*, vol. 4, no. 2, pp. 133–137, 2007.

[95] I. Papagiannouli, P. Aloukos, D. Rioux, M. Meunier, and S. Couris, "Effect of the composition on the nonlinear optical response of Au_xAg_{1-x} nano-alloys," *Journal of Physical Chemistry C*, vol. 119, no. 12, pp. 6861–6872, 2015.

[96] M. Vinod and K. Gopchandran, "Au, ag and au:ag colloidal nanoparticles synthesized by pulsed laser ablation as sers substrates," *Progress in Natural Science: Materials International*, vol. 24, no. 6, pp. 569 – 578, 2014.

[97] G. Compagnini, E. Messina, O. Puglisi, and V. Nicolosi, "Laser synthesis of Au/Ag colloidal nano-alloys: Optical properties, structure and composition," *Applied Surface Science*, vol. 254, no. 4, pp. 1007–1011, 2007.

[98] G. Compagnini, E. Messina, O. Puglisi, R. S. Cataliotti, and V. Nicolosi, "Spectroscopic evidence of a core-shell structure in the earlier formation stages of Au-Ag nanoparticles by pulsed laser ablation in water," *Chemical Physics Letters*, vol. 457, no. 4-6, pp. 386–390, 2008.

[99] K. J. M. Bishop, C. E. Wilmer, S. Soh, and B. A. Grzybowski, "Nanoscale forces and their uses in self-assembly," *Small*, vol. 5, no. 14, pp. 1600–1630, 2009.

[100] P. K. Jain and M. A. El-Sayed, "Plasmonic coupling in noble metal nanostructures," *Chemical Physics Letters*, vol. 487, no. 4, pp. 153 – 164, 2010.

[101] D. Rioux, S. Vallières, S. Besner, P. Muñoz, E. Mazur, and M. Meunier, "An analytic model for the dielectric function of Au, Ag, and their Alloys," *Advanced Optical Materials*, vol. 2, no. 2, pp. 176–182, 2014.

[102] O. Peña-Rodríguez, M. Caro, A. Rivera, J. Olivares, J. M. Perlado, and A. Caro, "Optical properties of Au-Ag alloys: An ellipsometric study," *Optical Materials Express*, vol. 4, no. 2, pp. 403–410, 2014.

[103] B. Johs and J. S. Hale, "Dielectric function representation by B-splines," *physica status solidi (a)*, vol. 205, pp. 715–719, apr 2008.

[104] Y. Nishijima and S. Akiyama, "Unusual optical properties of the Au/Ag alloy at the matching mole fraction," *Optical Materials Express*, vol. 2, no. 9, pp. 1226–1235, 2012.

END